





RESEARCH ARTICLE | JULY 25 2024

Electric-field induced phase separation and dielectric breakdown in *leaky* dielectric mixtures: Thermodynamics and kinetics

Haodong Zhang ; Fei Wang  ; Britta Nestler 



J. Chem. Phys. 161, 044704 (2024)

<https://doi.org/10.1063/5.0203527>



APL Quantum
Latest Articles Now Online
Read Now



Electric-field induced phase separation and dielectric breakdown in *leaky* dielectric mixtures: Thermodynamics and kinetics

Cite as: J. Chem. Phys. 161, 044704 (2024); doi: 10.1063/5.0203527

Submitted: 14 February 2024 • Accepted: 3 July 2024 •

Published Online: 25 July 2024



View Online



Export Citation



CrossMark

Haodong Zhang,^{1,2}  Fei Wang,^{1,2,a)}  and Britta Nestler^{1,2,3} 

AFFILIATIONS

¹Institute of Applied Materials-Microstructure Modelling and Simulation, Karlsruhe Institute of Technology, Straße am Forum 7, 76131 Karlsruhe, Germany

²Institute of Nanotechnology, Karlsruhe Institute of Technology, Hermann-von-Helmholtz-Platz 1, 76344 Eggenstein-Leopoldshafen, Germany

³Institute of Digital Materials Science, Karlsruhe University of Applied Sciences, Moltkestraße 30, 76133 Karlsruhe, Germany

^{a)}Author to whom correspondence should be addressed: fei.wang@kit.edu

ABSTRACT

Dielectric materials form the foundation of many electronic devices. When connected to a circuit, these materials undergo changes in microscopic morphology, such as the demixing of dielectric mixtures through phase separation and dielectric breakdown, resulting in the formation of micro-filaments. Consequently, the macroscopic properties and lifespan of the devices are significantly altered. To comprehend the physical mechanisms behind it, we conducted a systematic investigation of the thermodynamics of multicomponent *leaky* dielectric materials. Beginning with the total energy functional, we derived expressions for the binodal composition, spinodal composition, and critical points. Furthermore, we constructed and validated theoretical phase diagrams for the binary leaky dielectric mixture, incorporating three crucial freedoms: composition, temperature, and electric field strength. In addition, we analyzed the equilibrium interfacial tension impacted by the electric field and studied the dynamic aspects of dielectric materials, examining two morphological transformations: electrostriction and dielectric breakdowns. Our analysis unveiled a connection between these dynamic phenomena and the electric field-induced interfacial instability. The present work is expected to be supportive of future research on multicomponent dielectric materials by offering a comprehensive understanding of their thermodynamic and kinetic behaviors.

© 2024 Author(s). All article content, except where otherwise noted, is licensed under a Creative Commons Attribution-NonCommercial 4.0 International (CC BY-NC) license (<https://creativecommons.org/licenses/by-nc/4.0/>). <https://doi.org/10.1063/5.0203527>

I. INTRODUCTION

Dielectric materials play a crucial role in electronic devices, finding widespread applications in fields such as batteries,^{1,2} microwave communication systems,^{3,4} semiconductor,^{5,6} and energy storage.^{7,8} In the operation of these devices, microscopic phase transformation often occurs^{9,10} and usually leads to significant changes in the macroscopic properties. Some phase transformations are desirable, such as the reported enhancement of thermal conductivity through the electric field-induced phase separation (EIPS) of dielectric materials,^{11,12} while others, such as dielectric breakdown,^{13,14} may be less preferred as they can reduce

device lifespan or lead to equipment failure. It is the consensus that electric field induced instability is a key factor contributing to these changes in the microscopic morphologies and subsequent macroscopic property alterations.^{15–17} On the one hand, the study of electric field-induced interface instability dates back to the seminal contributions of Taylor and Melcher.^{18–20} In their approach, the everlasting thermal noises perturb the interface, resulting in the inhomogeneous interface charges, in turn, leading to the Coulomb and dielectric forces, which are unbalanced by the interfacial tension. Hence, electric field-related forces deform the interface and cause interfacial instability. On the other hand, the EIPS of the dielectric mixture can give rise to another instability.^{21,22}

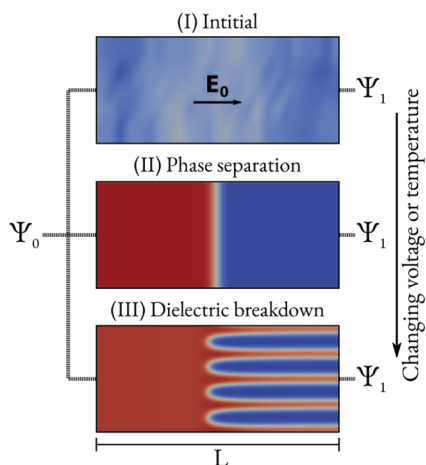


FIG. 1. (a) Initial simulation setup with the perturbed homogeneous binary dielectric mixture. The electric potentials on the left and right boundaries are denoted by Ψ_0 and Ψ_1 , respectively. The external electric field strength is $|\mathbf{E}_0| = (\Psi_1 - \Psi_0)/L$. (b) Changes in the electric field or temperature can induce phase separation, generating the droplet (red) and matrix (blue) phases. (c) Electric-field triggers the interfacial instability and dielectric breakdown.

Triggered by the thermal noises, as shown in Fig. 1(a), the electric field alters the total energy of the homogeneous dielectric mixture. With changing the electric field, or altering the temperature, the demixing into several distinct phases takes place via the so-called spinodal decomposition mechanism, which is shown in Fig. 1(b). Due to the different permittivities and conductivity, these phases can change morphology via diffusion and convection, forming various microstructures, including layers, bi-continuous structure, and dispersed droplets/particles.^{23–25} With a further change in electric field and temperature, the separated phases may experience interfacial instabilities, forming filament structures connecting the anode with the cathode; see Fig. 1(c). This phenomenon is called the dielectric breakdown (DB), which drastically dysfunctions the electronic device. To understand the origin and underlying physical mechanisms of electric field-induced instability phenomena, it is essential to have a concise and meticulous notion of thermodynamics, which guides us to the equilibrium state of the multicomponent dielectric materials.

In Ref. 26, the impact of electric fields on the perfect dielectric liquid–vapor system was discussed, focusing on shifting the vapor pressure and boiling point. The authors suggested the existence of dielectric pressure caused by the presence of an electrostatic field. They deduced the electrochemical potential inside the electric field, consequently modifying the vapor pressure. In this study, the equilibrium compositions of liquid and vapor phases are assumed to be unchangeable with increasing the electric field. This assumption may lead to some discrepancies. For instance, in the Li-ion intercalation materials discussed in Ref. 27, the equilibrium composition changes drastically inside the electric field. Moreover, the authors derived the thermodynamically consistent phase diagram of a binary *leaky* dielectric mixture through stability analysis, exploring variations in species composition under different external electric fields. They

also employed linear stability analysis to study the dynamics during electric field-induced phase separation of the dielectric mixture. The dispersion relation was used to obtain the spinodal composition, showing good agreement with the experimental results. Reference 28 focused on the fundamental thermodynamic quantities of the liquid–vapor system, such as Gibbs free energy and internal energy, expressed as functions of electric field strength. Considering the interplay of capillarity and the electric field, they proposed a theoretical model to estimate the equilibrium liquid mole fractions for ideal and non-ideal systems. In addition, the crucial role of the contact angle of the dielectric fluid on the electrode was discussed. In Ref. 29, the phase separation of a polymer blend inside an electric field was studied. Employing mean-field theory, the authors proposed a theoretical model for calculating the equilibrium condition of the polymer blends; the results were compared to those of molecular dynamic simulation. They reported that the spinodal decomposition of the polymer blend inside the electric field depends not only on the second derivative of permittivity to composition but also on the relative permittivity of individual species. In these studies for *leaky* dielectrics, the chemical equilibrium condition is addressed via the formulation of electrochemical potential coupled with the homogeneous electric field strength in the domain. However, for multi-component and multi-phase systems, the electrical steady state condition has not yet been fully clarified. In fact, because EIPS generates multiple phases with different conductivities and sizes, the external electric field can result in distinct electric field strengths inside each phase. Therefore, the non-uniform electric field in each phase results in modified total energy of the system, which not only guides the equilibrium compositions of the separated phases but also affects the critical point when EIPS takes place.

In this work, we focus on electric field-induced phase separation from the thermodynamic perspective. Starting from the total energy functional, we deduce the formulations for the equilibrium composition, spinodal composition, critical point, and critical electric field strength. The last factor plays the dominant role on EIPS at various temperatures. Notably, these theoretical values are carefully verified through phase-field simulations, which are based on the Cahn–Hilliard–Navier–Stokes–Gauss (CHNSG) model developed in our previous research.³⁰ By coupling the composition field with the electric field, we study EIPS by varying key parameters, including temperature, permittivity, conductivity, and electric field strength. Crucially, the immiscible gap and the spinodal region are not only changed by the composition-dependent permittivity but also were significantly influenced by the composition-dependent conductivity. This is of great importance for commercial intercalation materials in Li-ion battery applications,²⁷ such as Li_xCoO_2 ³¹ and $\text{Li}_{4+3x}\text{Ti}_5\text{O}_{12}$,³² where the conductivity may change in several orders via the metal-to-insulator transition. The enormous conductivity difference modifies the equilibrium electric field and, consequently, impacts the equilibrium composition field, a factor often overlooked in previous studies. In addition, our observations reveal that *leaky* dielectric materials exhibit two distinct connections to the electric field. By adjusting the co-action of permittivity and conductivity, the immiscible region enclosed by equilibrium compositions can either shrink or expand, resulting in the hindrance or facilitation of the electric field-induced phase separation.

Furthermore, based on thermodynamic information, we obtain the equilibrium interfacial tension γ —a critical parameter for analyzing interfacial instability and microscopic morphology transformations. We find that the electric field-induced shrinkage or expansion of the immiscible region can also influence γ , leading to either interfacial tension reduction (thinning) or increase (thickening). Particularly, the interfacial tension thinning effect is deeply associated with interfacial instability and contributes to our understanding of dielectric breakdown from a thermodynamic perspective. On the one hand, this may help us select the proper dielectric material and improve the device performance and reliability by avoiding DB. On the other hand, taking the advantages of DB, a better knowledge of the underlying mechanism can also be beneficial to design memristive devices that prefer controllable DB by the external electric field or temperature.³³

This paper is organized into distinct sections to facilitate a comprehensive presentation of our findings. The structure is delineated as follows: Section II introduces the total energy functional of the multi-component *leaky* dielectric fluid system. In addition, it outlines the numerical method employed for simulating the behavior of dielectric fluids. In Sec. III, we present the methodology to derive the equilibrium composition, spinodal composition, critical point, critical electric field strength, and interfacial tension pertinent to the binary *leaky* dielectric fluid when subjected to an electric field. A comparative analysis is undertaken in Sec. IV, aligning the numerical simulation with the theoretical calculation established in Sec. III. Particular emphasis is placed on presenting the phase diagram of the *leaky* dielectric fluid. Section V presents the interfacial tension, which is related to several pivotal phenomena, including electrostriction, and dielectric breakdown. The paper is concluded in Sec. VI.

II. DESCRIPTION OF THE MODEL

A. Total energy functional

For the multicomponent *leaky* dielectric system, the total energy functional, denoted as \mathcal{L} , exhibits spatial and temporal dependencies. This energy functional is composed of three primary components: the chemical free-energy functional represented by \mathcal{F} , the electric energy functional denoted as \mathcal{U} , and the macroscopic kinetic energy labeled as \mathcal{K} ,

$$\mathcal{L} = \mathcal{F}(\mathbf{x}, t, \mathbf{c}, \nabla \mathbf{c}) + \mathcal{U}(\mathbf{x}, t, \rho_e, \nabla \Psi) + \mathcal{K}(\mathbf{x}, t, \rho, \mathbf{u}).$$

1. Chemical free-energy functional

The chemical free-energy functional \mathcal{F} in the domain Ω is formulated by the sum of the bulk chemical free-energy density $f(\mathbf{c})$ and the gradient-related interfacial term as

$$\mathcal{F} = \int_{\Omega} g(\mathbf{c}, \nabla \mathbf{c}) \, d\Omega = \int_{\Omega} \left[f(\mathbf{c}) + \sum_{i=1}^N \frac{\kappa}{2} (\nabla c_i)^2 \right] d\Omega. \quad (1)$$

The interfacial tension parameter κ controls the scaling of interfacial tension. In this study, we employ the regular solution model for the bulk chemical free-energy density^{34,35} with

$$\frac{f(\mathbf{c})}{f^*} = T \sum_{i=1}^N c_i \ln c_i + \sum_{i<j}^{N,N} \chi_{ij} c_i c_j + \sum_{i<j<k}^{N,N,N} \chi_{ijk} c_i c_j c_k, \quad (2)$$

in which T represents temperature. The molecular interaction between components is characterized by the Flory parameter χ_{ij} , where $\chi_{ij} > 0$ indicates repulsion and vice versa. The triple interaction is influenced by the parameter χ_{ijk} for systems with more than two components. The reference free-energy density f^* is defined as $R_g T_r / v_m$ and is scaled by the gas constant R_g , reference temperature T_r , and molar volume v_m . We designate f^* as the unit upon non-dimensionalization.

2. Electric potential energy

The electric potential energy \mathcal{U} is taken into consideration when the system is situated within an electrostatic field,

$$\mathcal{U} = \int_{\Omega} u(\rho_e, \nabla \Psi) \, d\Omega = \int_{\Omega} \left[-\frac{\epsilon}{2} (\nabla \Psi)^2 + \rho_e \Psi \right] d\Omega. \quad (3)$$

The volume integral in Eq. (3) comprises two aspects. One originates the energy density of the electric field and is associated with the material permittivity $\epsilon = \sum_{i=1}^N \epsilon_i c_i$. Here, ϵ_i represents the permittivity of component i . The other term $\rho_e \Psi$ denotes the energy required to place the charge density ρ_e onto the electric potential Ψ . In this work, the *leaky* dielectric model is adopted,^{19,36} where the nonzero conductivity is assigned for each component. It implies that ρ_e describes the charge carrier density, which exists in the *leaky* dielectric material and contributes to the conductivity. The concept of ρ_e in *leaky* dielectric materials is consistent with previous studies.^{26–28}

3. Kinetic energy

The kinetic energy incorporates the constant density ρ and the macroscopic fluid flow velocity \mathbf{u} , yielding

$$\mathcal{K} = \int_{\Omega} \frac{\rho \mathbf{u}^2}{2} \, d\Omega. \quad (4)$$

B. Governing equation

In this study, we employ the Cahn–Hilliard–Navier–Stokes–Gauss model (CHNSG) previously developed in our previous work³⁰ to explore the thermodynamics of the multi-component dielectric fluid system in conjunction with electro-hydrodynamics.

1. Composition conservation

To characterize the spatiotemporal evolution of the composition for each component i , denoted as c_i , we adopt the Cahn–Hilliard equation, expressed as

$$\frac{\partial c_i}{\partial t} + \mathbf{u} \cdot \nabla c_i = \nabla \cdot \left(\sum_{j=1}^N M_{ij} \nabla \mu_j + \xi_i \right), \quad (5)$$

where the mobility $\mathbf{M} := (M_{ij}) \in \mathbb{R}^{N \times N}$ following Onsager's relation³⁷ is scaled by the reference interdiffusivity D^* , formulated as $(D^*/f^*)c_i (\delta_{ij} - c_j)$ (see the derivation in Ref. 38), where δ_{ij} is the Kronecker delta. Notably, the electrochemical potential μ_i is defined by the functional derivative of \mathcal{L} to c_i , leading to

$$\mu_i = \frac{\delta g}{\delta c_i} + \frac{\delta u}{\delta c_i} = \frac{\partial f}{\partial c_i} - \kappa \nabla^2 c_i - \frac{1}{2} \frac{\partial \epsilon}{\partial c_i} \mathbf{E}^2. \quad (6)$$

Here, $\mathbf{E} = -\nabla\Psi$ represents the local electric field strength, which is curl-free, so that the electromagnetism is not considered in this work. Consequently, the electrochemical potential is decided by both the chemical free-energy density g and the electric energy density u , underscoring the inherent coupling between the concentration field and the electric field.

In Eq. (5), the composition noise ξ is added to initiate the spinodal decomposition, following the fluctuation–dissipation theorem^{39,40} as

$$\langle \xi_i, \xi'_i \rangle = \frac{2M_{ii}f^*}{\Delta t} \nabla^2 \delta(\mathbf{x} - \mathbf{x}') \delta(t - t'),$$

where δ denotes Dirac's delta and Δt stands for the time step of the simulation. The numerical accuracy and stability of the stochastic phase-field model are expounded upon in our previous study.⁴⁰

2. Charge conservation

In the *leaky* dielectric approach, the identity of the charge carrier is not specified. In this way, the conservation equation for the spatiotemporal charge density ρ_e is needed and coupled with Gauss's law through the following set of equations:

$$\nabla \cdot (\epsilon \mathbf{E}) = \rho_e, \quad (7)$$

$$\frac{\partial \rho_e}{\partial t} + \mathbf{u} \cdot \nabla \rho_e = \nabla \cdot (\sigma \nabla \Psi). \quad (8)$$

In these equations, the material-dependent conductivity is denoted as $\sigma = \sum_{i=1}^N \sigma_i c_i$ and governs the charge kinetic behavior, where σ_i represents the conductivity of component i .

3. Momentum conservation

For the fluid flow velocity \mathbf{u} in Eqs. (5) and (8), the incompressible Navier–Stokes equations are adopted as

$$\nabla \cdot \mathbf{u} = 0, \quad (9)$$

$$\rho \left(\frac{\partial \mathbf{u}}{\partial t} + \mathbf{u} \cdot \nabla \mathbf{u} \right) = -\nabla p - \sum_{i=1}^N c_i \nabla \mu_i - \rho_e \nabla \Psi + \nabla \cdot \left[\eta (\nabla \mathbf{u} + \nabla \mathbf{u}^T) \right], \quad (10)$$

in which the pressure p is solved under the incompressible condition of Eq. (9). The second and third term in the right hand side of Eq. (10) denote the thermodynamic force and the Coulomb force, respectively. The detailed deduction is documented in our previous work.³⁰ The viscosity η plays a key role in governing the kinetic energy dissipation through the viscous effect.

In addition to the interpretation of the forces as potential gradients, the second and third terms on the right hand side of Eq. (10) can also be expressed by the thermodynamic stress tensor $\underline{\underline{\Theta}}$ and electrostatic Maxwell stress tensor $\underline{\underline{\sigma}}^M$ as

$$\begin{aligned} -\sum_{i=1}^N c_i \nabla \mu_i - \rho_e \nabla \Psi &= -\nabla \cdot (\underline{\underline{\Theta}} + \underline{\underline{\sigma}}^M), \\ \underline{\underline{\Theta}} &= -\left(g - \sum_{i=1}^N \frac{\delta g}{\delta c_i} c_i \right) \mathbf{I} + \sum_{i=1}^N \frac{\partial g}{\partial \nabla c_i} \otimes \nabla c_i, \\ \underline{\underline{\sigma}}^M &= -\left(u - \sum_{i=1}^N \frac{\delta u}{\delta c_i} c_i - \frac{\delta u}{\delta \rho_e} \rho_e \right) \mathbf{I} - \frac{\partial u}{\partial \nabla \Psi} \otimes \nabla \Psi. \end{aligned}$$

Both interpretations are mathematically equivalent. The detailed derivations is documented in our previous work.³⁰

4. Discretion method and boundary condition

The governing equations, Eqs. (5)–(10), are discretized by using the finite difference method, as depicted in Ref. 30 with Message Passing Interface (MPI) techniques. The non-dimensionalization process employs characteristic length $x^* = 10^{-8}$ m, reference diffusivity $D^* = 10^{-9}$ m²/s, reference free-energy density $f^* = 10^6$ N/m², and electric field strength $\mathbf{E}^* = 10^8$ V/m. The non-dimensionalization procedure follows the methodology presented in Ref. 37.

To the Cahn–Hilliard–Navier–Stokes–Gauss model, we apply the following boundary conditions as

- (i) Neumann boundary condition for the composition c_i and electrochemical potential μ_i for each component i as:

$$\nabla c_i \cdot \mathbf{n} = 0, \quad \nabla \mu_i \cdot \mathbf{n} = 0.$$

For the non-zero Neumann boundary condition and the associated chemical wall free energy, we refer to Ref. 41.

- (ii) Dirichlet boundary condition is applied for the electric potential Ψ on the left and right boundaries,

$$\Psi_{\text{left}} = \Psi_0, \quad \Psi_{\text{right}} = \Psi_1, \quad (11)$$

while no-flux boundary condition is added on the other sides,

$$\nabla \Psi \cdot \mathbf{n} = 0.$$

This setup models the scenario of putting a dielectric mixture into two electrodes with voltage drops. Since the *leaky* dielectric is considered as the resistance R that changes with composition c , the charge current $I = (\Psi_{\text{right}} - \Psi_{\text{left}})/R$ is also composition-dependent, following the Ohm's law according to Eq. (8).

In another scenario, for instance, the dielectric mixture in the AC circuit, or the charging battery, the time-relevant charge current $I(t)$ may flow across the electrode surface Γ (boundaries) as

$$I(t) = \int_{\Gamma} \sigma(c) \nabla \Psi \cdot \mathbf{n} d\Gamma,$$

so that

$$I_{\text{left}} = I_{\text{right}} = I_{\text{const}}. \quad (12)$$

Hence, the time-relevant electric potential on the left and right boundaries will change with the composition c on the electrodes. The voltage drop is constrained by Ohm's law as $\Psi_{\text{right}} - \Psi_{\text{left}} = I R$.

Either Eq. (11) or Eq. (12) is sufficient to solve the second order partial differential equation of Gauss' law, Eq. (7). In this work, we focus on the applied constant voltage drop onto the dielectric mixture, as the setup in previous studies^{26,27} and shown in Fig. 1.

- (iii) No-slip boundary condition is used for the velocity \mathbf{u} . The numerical convergence of the CHNSG model has been extensively discussed in our previous study.³⁰

III. THERMODYNAMIC EQUILIBRIUM

To specify the real physical system that could be studied with the introduced phase-field framework in Sec. II B, we choose the ion intercalation material $\text{Li}_{4x+3}\text{Ti}_5\text{O}_{12}$, which has been widely investigated for Li-ion batteries^{42,43} and memristive devices.^{44,45} Figure 1 provides an illustration of the setup. Due to the stoichiometry of $\text{Li}_{4x+3}\text{Ti}_5\text{O}_{12}$ controlled by the coefficient x , the homogeneous phase shown in Fig. 1(a) may become thermodynamically unstable. By applying an electric-field drop $\Psi_1 - \Psi_0$ on to it, the thermal noise triggers composition fluctuation, leading to phase separation and the formation of two distinct phases, as represented by the red-colored $\text{Li}_7\text{Ti}_5\text{O}_{12}$ and the blue-colored $\text{Li}_4\text{Ti}_5\text{O}_{12}$ shown in Fig. 1(b). Because of the low conductivity of $\text{Li}_4\text{Ti}_5\text{O}_{12}$, the separated phases build the resistance with a constant weak current flowing through. With a further change in Ψ_1 or temperature T , the interface becomes unstable and the microscopic fingering of $\text{Li}_7\text{Ti}_5\text{O}_{12}$ with high conductivity connects the electrodes and results in the effective dielectric breakdown (DB) shown in Fig. 1(c). Macroscopically, the system proceeds with the insulator-metal transition controlled by the electric field that has potential to be applied for neuromorphic computing.⁴⁴

In addition to $\text{Li}_{4x+3}\text{Ti}_5\text{O}_{12}$, other materials, such as Li_xCoO_2 ³¹ and $\text{Li}_x\text{Ni}_{1/3}\text{Co}_{1/3}\text{Mn}_{1/3}\text{O}_2$,⁴⁶ also undergo similar phase transitions inside the electric field in a more complex manner. Here, the phase transition is not directly controlled by altering the electric field, but decided by the operational conditions on the boundary, such as the ion inserting rate into the material. This scenario can be understood as the current $I(t)$ trespassing the material, which alters the electric field by Ohm's law. To understand the critical phenomena that occur in these materials, but are not limited in these materials, we adopt the *leaky* dielectric model and scrutinize the criteria of the critical morphological transformations from the thermodynamic perspective. The thermodynamic equilibrium of the entire system is determined by the interplay of two conditions, namely, the electrical steady state and the chemical equilibrium. Without losing the generality, the derivation for the thermodynamic equilibrium is conducted for a binary droplet–matrix system. Omitting the subscript i for multicomponent cases, we use c to represent the droplet composition, so that the matrix composition is $1 - c$. The droplet electrochemical potential is denoted as μ .

A. Electric field at steady state

On the one hand, Eq. (8) gives rise to $\partial\rho_e/\partial t = 0$, which defines the electrical steady state and is equivalent to Ohm's law^{27,36} as

$$\begin{aligned} \nabla \cdot \mathbf{J} &= 0, \\ -\sigma \nabla \Psi &= \sigma \mathbf{E} = \mathbf{J}. \end{aligned} \quad (13)$$

In this work, we assume that during the microstructure evolution, the steady state of charge density is reached in a more rapid manner than the diffusion of material. Hence, the charge density flux \mathbf{J} is constant at every position inside the domain. With time evolving, the composition c changes the material-dependent conductivity $\sigma(c)$, as reported in Ref. 47 for the $\text{Li}_{4x+3}\text{Ti}_5\text{O}_{12}$ phase. Hence, the charge density flux \mathbf{J} is also modified. In this way, the steady state is also influenced by the chemical equilibrium. Here,

the electric steady state of dielectric mixtures is categorized into two groups.

- (i) For the non-phase separated homogeneous mixture, as shown in Fig. 1(a), the uniform composition c gives rise to the constant \mathbf{E} equals to the external electric field strength \mathbf{E}_0 . In this case, Ohm's law results in the composition dependent flux,

$$\mathbf{J}(c) = \sigma(c)\mathbf{E}_0,$$

so that the mixture functions as a resistance with a constant resistivity proportional to $1/\sigma(c)$.

- (ii) Once electric field-induced phase separation happens, two distinct phases appear, as shown in Fig. 1(b). The electric field strength in different phases becomes composition-dependent as

$$\mathbf{E}(c) = \frac{\mathbf{J}}{\sigma(c)}. \quad (14)$$

In this case, the system is regarded as the serial resistance of red droplet and blue matrix phases. Not only the conductivity $\sigma(c)$ but also the thickness of each phase significantly influences the whole resistance. In Sec. IV A 3, Eq. (14) will be carefully validated. This crucial relationship reflects the fact that the electrical steady state can also influence the chemical equilibrium in return.

B. Binodal composition

On the other hand, Eq. (5) points out the chemical equilibrium condition $dc/dt = 0$, indicating the equal electrochemical potential μ for the entire system. For non-phase separated mixtures, the homogeneous composition c guarantees a uniform chemical potential μ . In this work, we assume the permittivity ϵ to be the linear function of composition. Hence, the equilibrium composition does not change by the electric field. While for mixtures proceeding EIPS, the chemical equilibrium is described by the binodal compositions as follows: we integrate μ of Eq. (6) inside the bulk region, from the droplet equilibrium composition c_d to the matrix equilibrium composition c_m , yielding

$$\begin{aligned} \Delta f(c_d) + \Delta u(c_d) - \mu^e(c_d)(c_d - c_m) &= 0, \\ \mu(c_d) &= \left. \frac{\partial f}{\partial c} \right|_{c=c_d} - \frac{1}{2} \frac{\partial \epsilon}{\partial c} \mathbf{E}_d^2, \\ \mu(c_m) &= \left. \frac{\partial f}{\partial c} \right|_{c=c_m} - \frac{1}{2} \frac{\partial \epsilon}{\partial c} \mathbf{E}_m^2, \\ \mu(c_d) &= \mu(c_m) = \mu^e, \end{aligned} \quad (15)$$

where the excess total energy density is denoted by $\Delta f + \Delta u - \mu^e \Delta c$, including the excess chemical energy density $\Delta f = f(c) - f(c_m)$ and the excess electric energy density Δu with expression in Eq. (18). The equilibrium electrochemical potential represented by μ^e and Δc is defined as $(c - c_m)$. The electric field strengths within the equilibrium phases, \mathbf{E}_d and \mathbf{E}_m , are determined by Eq. (13). Since the separated phases build a serial resistance, as shown in Fig. 1(b),

the electric field strength in each phase can be calculated with the boundary condition for the electric field,

$$\int_0^{L_0} \mathbf{E}_d \, dn + \int_{L_0}^L \mathbf{E}_m \, dn = \mathbf{E}_0 L = \Psi_0 - \Psi_1. \quad (16)$$

At the equilibrium state, the electric field strength inside each phase is constant and is determined with the phase thickness that is associated with the interface position L_0 . Here, \mathbf{E}_0 denotes the external electric field strength, as shown in Fig. 1, differing from the local electric field strength \mathbf{E} . Consequently, the composition-dependent \mathbf{E} induces a variation in the electrochemical potential μ , which, in turn, modifies the equilibrium compositions c_d and c_m due to the influence of the electric field. This relationship will be thoroughly examined in Sec. IV A.

In addition, the excess electric energy density needs to be computed for two different conditions separately: (i) for non-phase separated mixtures, the constant $\mathbf{E} = \mathbf{E}_0$ gives rise to

$$\Delta u = -\frac{\varepsilon(c)}{2} \mathbf{E}^2; \quad (17)$$

(ii) for phase-separated mixtures, the excess electric energy density reads

$$\Delta u(c) = \int_{c_m}^c -\frac{1}{2} \frac{\partial \varepsilon}{\partial c} \mathbf{E}^2(c) \, dc. \quad (18)$$

C. Spinodal composition

With the above-mentioned equilibrium conditions, we now consider the critical criterion for the electric field-induced phase separation. The spinodal decomposition is regarded as one of the most crucial mechanisms and is discussed in this work. Based on the electrochemical potential μ defined in Eq. (6), the impact of electric field on the spinodal composition, denoted as c_s , is expressed as

$$\begin{aligned} \frac{\partial^2(\Delta f + \Delta u - \mu^e \Delta c)}{\partial c^2} &= \frac{\partial^2 f}{\partial c^2} - \frac{\partial \varepsilon}{\partial c} \frac{\partial \mathbf{E}}{\partial c} \cdot \mathbf{E} - \frac{1}{2} \frac{\partial^2 \varepsilon}{\partial c^2} \mathbf{E}^2 \\ &= \frac{\partial^2 f}{\partial c^2} - \frac{\partial \varepsilon}{\partial c} \frac{\partial \mathbf{E}}{\partial c} \cdot \mathbf{E} = 0. \end{aligned} \quad (19)$$

Given the assumption that the permittivity ε follows a linear function of c , the second derivative vanishes as $\partial^2 \varepsilon / \partial c^2 = 0$. Hence, the electric field strength decides the phase separability of the dielectric mixture. (i) For a non-separable mixture, $\mathbf{E} = \mathbf{E}_0$ does not depend on c . Therefore, the spinodal composition is not varied by the electric field as

$$\left. \frac{\partial \mu}{\partial c} \right|_{c=c_s} = \frac{\partial^2 f}{\partial c^2} = 0. \quad (20)$$

(ii) Once phase separation happens, the spinodal composition is drastically modified by the electric field. Substituting Eq. (14) into Eq. (19), the spinodal composition c_s is determined by

$$\begin{aligned} \left. \frac{\partial \mu}{\partial c} \right|_{c=c_s} &= \frac{\partial^2 f}{\partial c^2} - \frac{\partial \varepsilon}{\partial c} \left(\frac{\partial \mathbf{E}}{\partial c} \frac{\partial \sigma}{\partial c} \right) \cdot \mathbf{E} \\ &= \frac{\partial^2 f}{\partial c^2} + \frac{\partial \varepsilon}{\partial c} \frac{\partial \sigma}{\partial c} \frac{\mathbf{E}^2}{\sigma} = 0. \end{aligned} \quad (21)$$

Crucially, Eq. (21) highlights the pivotal notion that the electric field strength \mathbf{E} of the multi-component system is contingent upon the composition c . This enables us to study the electric field-induced phase separation and will be expounded upon in Sec. IV B. The linear function of $\varepsilon(c)$ constitutes a phenomenological treatment; more intricate formulations, such as exponential and higher-order polynomial functions, can delicately modify the spinodal composition, primarily due to the presence of the term $\partial^2 \varepsilon / \partial c^2 \neq 0$. More details are found in Ref. 27 where the linear stability of the spinodal decomposition is carried out.

D. Critical point

Following the definition of spinodal composition, the critical point and critical temperature can be determined through the condition that the equation,

$$\frac{\partial^2 f}{\partial c^2} + \frac{\partial \varepsilon}{\partial c} \frac{\partial \sigma}{\partial c} \frac{\mathbf{E}_0^2}{\sigma} = 0, \quad (22)$$

possesses a unique solution c^* within the interval (0, 1). Utilizing the regular solution formulation for the chemical free-energy density, denoted as $f(c)$ in Eq. (2) and the linear function of conductivity σ to c in Eq. (21) can be simplified into a cubic polynomial amenable to a solution using the Cardano formula. As an example in the binary system in this study, with $|\mathbf{E}_0| = 0.10$, $\partial \varepsilon / \partial c = 39$, $\partial \sigma / \partial c = 4$, the critical temperature is $T^* = 1.76103$ and the critical composition is $c^* = 0.5119$. For more complicated scenarios, the critical point necessitates numerical computation. Rewriting Eq. (22), the critical electric-field strength to induce phase separation is expressed as

$$|\mathbf{E}_c| = \sqrt{-\frac{\partial^2 f / \partial c^2}{(\partial \varepsilon / \partial c)(\partial \ln \sigma / \partial c)}}. \quad (23)$$

E. Interfacial tension

To explain the electric field-induced dielectric breakdown, we derive the interfacial tension of the droplet–matrix system inside the electric field as in the following. Initially, we examine the thermodynamic equilibrium condition for any composition c ,

$$\frac{\partial f}{\partial c} + \frac{\partial u}{\partial c} - \kappa \nabla^2 c = \mu^e. \quad (24)$$

Hence, the excess total energy density equates to

$$\Delta f + \Delta u - \mu^e \Delta c = \frac{\kappa}{2} (\nabla c)^2.$$

Integrating it along the interface's normal direction from $n = 0$ to $n = L$, the droplet–matrix interfacial tension inside the electric field reads

$$\begin{aligned} \gamma &= \int_0^L \left[\Delta f + \Delta u - \mu^e \Delta c + \frac{\kappa}{2} (\nabla c)^2 \right] dn \\ &= 2 \int_0^L \left[\Delta f + \Delta u - \mu^e \Delta c \right] dn. \end{aligned} \quad (25)$$

This integral can only be evaluated numerically. More details about the above-mentioned derivations are documented in A. Further elucidation on the interfacial tension and its associated behaviors will be provided in Sec. IV D.

TABLE I. List of parameters adopted in simulations.

Parameter	Description	Value
χ_{12}	Flory parameter	3.78
κ	Interfacial tension parameter	4.0
ϵ_2	Matrix permittivity	1.0
ν	Permittivity ratio	
σ_2	Matrix conductivity	1.0
s	Conductivity ratio	
Ψ_0	Electric potential on left boundary	0.0
$ \mathbf{E}_0 $	External electric field strength magnitude	0.1
ρ	Density	1.0
η	Viscosity	1.0
M	Mobility	1.0
Δt	Simulation time step	0.001
ξ	2D thermal noise	(0.01, 0.01)

IV. DISCUSSION

In this section, we first validate the thermodynamic quantities of the binary dielectric fluid defined in Sec. III with phase-field simulation. The essential parameters utilized in the simulations are presented in Table I, accompanied by their non-dimensionalization using the characteristic values expounded in Sec. II B 4. To avoid redundancy, we define the permittivity ratio as $\nu = \epsilon_1/\epsilon_2$ and the conductivity ratio as $s = \sigma_1/\sigma_2$.

A. Validation of equilibrium composition

In this part, our focus is on assessing the influence of the electric field on the droplet–matrix equilibrium composition. We specifically examine three permittivity ratios, denoted as $\nu = 1 : 40$, $20 : 1$, and $40 : 1$. For each ν , simulations encompass a range of temperatures T ranging from 1.0 to 1.8. The initial configuration is identical to that shown in Fig. 1. At the given temperature T , the initial compositions align with the electric-field-free equilibrium

compositions, which locate on the black dashed binodal line shown in Fig. 2(a).

1. Permittivity

Clearly discernible in Fig. 2(a) (i), we observe a gradual change in the equilibrium composition profile along the droplet–matrix interface with the black dashed c -profile under the electric-field-free condition reveals two distinct behaviors in composition variances. (I) For $\nu > 1$, signifying the droplet permittivity larger than that of the matrix, the droplet equilibrium composition c_d decreases, becoming smaller than the electric-field-free c_d , while the matrix equilibrium composition c_m increases, exceeding the electric-field-free c_m . In addition, the slope of the composition profile at the interface ($x = 100$) diminishes with increasing $\nu > 1$. (II) For $\nu < 1$, the scenario is reversed, revealing a stiffer interface composition profile in comparison to the black dashed electric-field-free c represented by the red dotted–dashed line.

Despite the pronounced alterations in equilibrium composition, the electric potential Ψ demonstrates only subtle differences with the distinct ν , as shown in Fig. 2(b) (ii). According to Eq. (14), the electric field within the dielectric fluid depends significantly on the conductivity σ . Considering $\sigma = \sum_{i=1}^N \sigma_i c_i$, the composition variance induced by the permittivity exerts a weak influence on σ . Consequently, Ψ is slightly altered by ν at a given temperature. However, when the temperature T shown in Fig. 2(c) changes evidently, both the composition profile and the electric field undergo significant modifications. Even at $T = 1.8$, the droplet–matrix interface disappears, indicating fluid remixing by the electric field.

As the droplet–matrix binary phase diagram Fig. 2(a) presents, for various permittivity ratios ν and temperatures T , the simulated binodal compositions (colored dots) align well with theoretical values (colored lines) derived from Eq. (15). Notably, the immiscible region enclosed by the colored binodal shows the positive correlation with the permittivity ratio. To explain this observation, we rewrite the electric energy density of Eq. (18) as

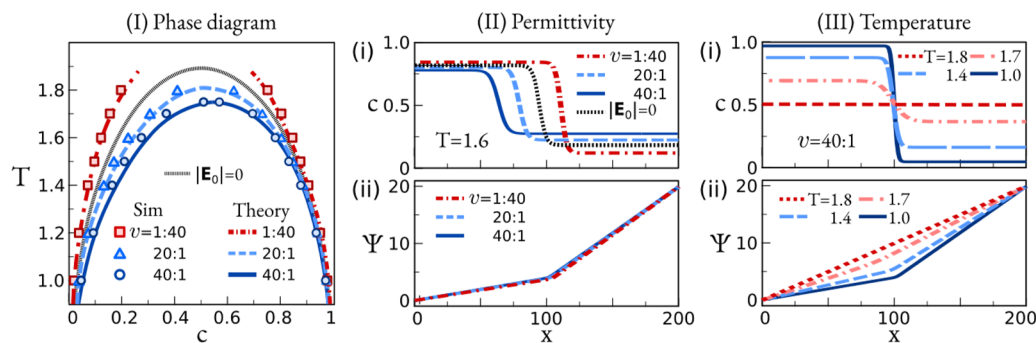


FIG. 2. Thermodynamic equilibrium of the droplet–matrix system inside the electric field. (a) Phase diagram by different droplet–matrix permittivity ratios $\nu = \epsilon_d/\epsilon_m$. Color dots: simulated equilibrium composition; color lines: theoretical binodal composition with Eq. (15). Black dashed line: equilibrium composition without an external electric field. (b) Permittivity significantly influences, (i) equilibrium composition distribution across the droplet–matrix interface (shifted for better demonstration), but only slightly changes and (ii) equilibrium electric potential. Temperature is set constant at $T = 1.6$. (c) Temperature impacts both (i) equilibrium composition distribution and (ii) equilibrium electric potential. Here, the permittivity ratio is fixed as $\nu = 40 : 1$.

$$\Delta u(c) = -\frac{J^2}{2} \frac{\partial \varepsilon}{\partial c} \frac{c - c_m}{\sigma(c)\sigma_m}, \quad (26)$$

and we find the permittivity ratio impacts the electric energy density becoming straightforward. For $\nu > 1$, *per se* $\partial \varepsilon / \partial c = \nu - 1 > 0$, Δu is non-positive, which reduces the excess total energy $\Delta f + \Delta u - \mu^e \Delta c$. According to Eq. (24), the interfacial energy term $\kappa(\nabla c)^2/2$ decreases, which flattens the droplet–matrix interface, encouraging the mixing of droplets with the matrix. Conversely, for $\nu < 1$, the electric field increases the excess total energy, thus sharpening the interface, and enhances the demixing of droplets with the matrix.

The transition point happens at $\nu = 1$, where the identical permittivity for droplet and matrix phases results in zero electric energy density changes. In addition, the electrochemical potential μ is uncoupled with the electric field strength. In this case, thermodynamic equilibrium exhibits no difference from the scenario of electric potential energy-free conditions. In other words, only chemical free-energy dominates the equilibrium.

An additional insight from the binary phase diagram is the heightened impact of the electric field at high temperatures. Because the chemical free-energy density Δf reduces significantly with rising temperature,⁴⁸ the excess electric energy density Δu tends to play a prominent role. At high temperature, the excess total energy $\Delta f + \Delta u - \mu^e \Delta c$ is vastly scaled with Δu , resulting in the huge binodal composition derivation from the equilibrium composition without the electric field.

2. Conductivity

As stated in Eq. (26), the conductivity also influences the electric energy density as well. To elucidate this, we vary the conductivity ratio $s = \sigma_1/\sigma_2$ between two phases from 1 : 5 to 10 : 1. The resulting equilibrium behaviors are shown in Fig. 3. As s rises, the electric field at the interface (gray-shaded region) transitions from a concave to a convex shape, with an inflection point occurring at $s = 1$, as guided by the black dashed line shown in Fig. 3(a). Consequently, the equilibrium compositions, shown in Fig. 3(b) undergo modifications, revealing an increase in the equilibrium matrix composition and a decrease in the equilibrium droplet composition with s . In other words, the droplet–matrix demixing is enhanced by the larger conductivity ratio. Furthermore, a reduction in s also leads to more induced charges at the interface, as shown in Fig. 3(c). Particularly for $s = 1$, the equilibrium compositions align with the binodal compositions in the absence of the electric field. This observation suggests that the induced charges at the interface do not affect the equilibrium.

3. Composition-dependent electric field strength

Subsequently, we study the thermodynamic equilibrium influenced by the external electric field strength $|\mathbf{E}_0|$. As shown in Fig. 4(a) (i), increasing $|\mathbf{E}_0|$ not only drastically reduces the composition difference between droplet and matrix phases but also widens the interface, as highlighted by the blue shaded region for $|\mathbf{E}_0| = 0.01$ and by the red shaded region for $|\mathbf{E}_0| = 0.20$. The effect of the electric field on the interface width will be discussed in Sec. IV D. With a further increase in $|\mathbf{E}_0|$, c_d , and c_m converges, as guided by the

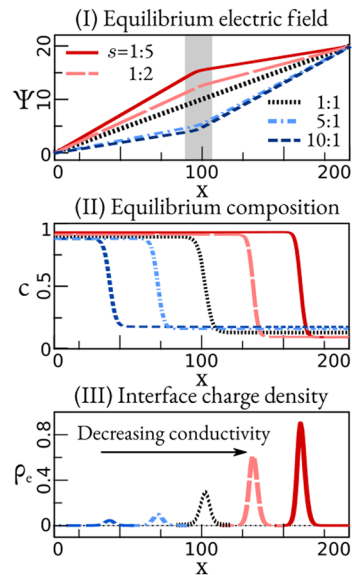


FIG. 3. Thermodynamic equilibrium of the droplet–matrix system at different droplet–matrix conductivity ratios $s = \sigma_1/\sigma_2$. (a) Equilibrium electric field along x direction. (b) Equilibrium composition. (c) Interface charge density. Both (b) and (c) are shifted in the x direction for better demonstration. Temperature is set constant at $T = 1.4$. The external electric field strength is $|\mathbf{E}_0| = 0.1$. The permittivity ratio is $\nu = 40 : 1$.

colored dots shown in Fig. 4(a) (ii). It indicates that the electric field promotes droplet–matrix mixing. Especially at $|\mathbf{E}_0| \geq 0.22$, droplet and matrix are miscible with each other and the interface disappears. This phenomenon leads to some interesting behaviors, which will be further discussed in Sec. IV E 2. In addition, the simulated binodal compositions are compared to the colored theoretical lines, affirming the accuracy of our theory Eq. (15).

Another concern pertains to the proposition of composition-dependent electric field strength, denoted as $\mathbf{E}(c)$ in Eq. (14). This formulation exerts a profound influence on thermodynamics in two dimensions. (I) Owing to the varying $\mathbf{E}(c)$ along the interface, the excess electric energy density Δu becomes composition dependent, as expressed in Eq. (26). To verify our theory, we compare the simulated $\mathbf{E}(c)$ and Δu to the theoretical lines derived from Eqs. (14) and (26) shown in Fig. 4(b). Despite some deviations in $\mathbf{E}(c)$, particularly at $T \leq 1.4$, the excess electric energy density Δu exhibits excellent agreement with our theory. This underscores the correct expression of Δu as per Eq. (18), rather than Eq. (17). (II) Given that \mathbf{E} is a function of composition c , its first derivative $\partial \mathbf{E} / \partial c$ is nonzero and significantly impacts the spinodal composition, as the calculation of the spinodal composition in Eq. (21). This aspect will be further heeded in Sec. IV B.

4. Interface orientation

In the derivation of the equilibrium condition, as Eq. (16), an assumption is posited that the local electric field strength \mathbf{E} at interface is parallel to the interface normal direction \mathbf{n} . To refine Eq. (18)

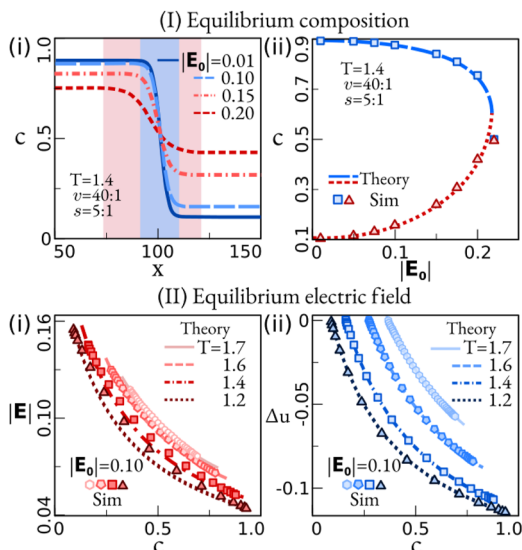


FIG. 4. Thermodynamic equilibrium of the droplet–matrix system with external electric field strength $|\mathbf{E}_0|$. (a) Equilibrium composition. (i) Composition profile along x direction. The color-shaded region depicts the interface region. (ii) Binodal composition. (b) The composition-dependent electric field at various temperatures T . (i) Electric field strength $\mathbf{E}(c)$ with composition c . Dots: simulation; lines: theory according to Eq. (14). (ii) Excess electric energy density Δu as a function of c . Dots: simulation; lines: theory according to Eq. (18).

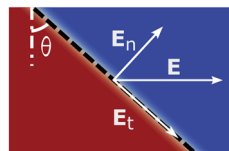


FIG. 5. Illustration of the droplet–matrix interface having the intersection angle θ with the local electric field strength \mathbf{E} at interface. The interface is marked by the black dashed line. \mathbf{E}_n and \mathbf{E}_t represent the composition of \mathbf{E} in the interface normal and tangent directions, respectively.

- (ii) The serial setup positions the droplet–matrix interface perpendicular to \mathbf{E}_0 , as shown in Fig. 6(b) (ii). Here, the electric field strength is decomposed into $\mathbf{E}_n = \mathbf{E}(c)$ in the normal direction and $\mathbf{E}_t = \mathbf{0}$ in the tangent direction. The material-dependent Ψ results in the equilibrium compositions differing from those in the parallel setup, as shown in Fig. 6(b) (iii). In this way, the excess electric potential Δu is expressed as

$$\Delta u(c) = \int_{c_m}^c -\frac{1}{2} \frac{\partial \varepsilon}{\partial c} (\mathbf{E} \cos \theta)^2 dc, \quad (28)$$

for the electric potential density difference Δu , we decompose \mathbf{E} into the interface normal and tangent directions (see Fig. 5) as $\mathbf{E}_n + \mathbf{E}_t$ and $\mathbf{E}_n \cdot \mathbf{E}_t = 0$, yielding

$$\Delta u = \int_0^x -\frac{1}{2} \frac{\partial \varepsilon}{\partial c} (\mathbf{E}_n^2 + \mathbf{E}_t^2) \nabla c \cdot d\mathbf{n},$$

which indicates the significant importance of the intersection angle between \mathbf{E} and \mathbf{n} , which is denoted as θ . To elucidate the interface orientation effect on the equilibrium, we scrutinize two distinct configurations.

- (i) The parallel configuration with $\mathbf{n} \parallel \mathbf{E}_0$ is exemplified in Fig. 6(a) (i), which results in $\mathbf{E}_n = \mathbf{0}$ and $\mathbf{E}_t = \mathbf{E}_0$. At equilibrium, the electric potential Ψ and \mathbf{E} show no material dependency, as shown in Fig. 6(a) (ii). The excess total energy density governing the equilibrium can be written as

$$\begin{aligned} \Delta f + \Delta u - \mu^e \Delta c &= \Delta f - f'(c_m) \Delta c - \frac{\mathbf{E}^2}{2} \left[\varepsilon(c) - \varepsilon_m - \frac{\partial \varepsilon}{\partial c} \Delta c \right] \\ &= \Delta f - f'(c_m) \Delta c. \end{aligned} \quad (27)$$

Thus, the equilibrium compositions c_d and c_m coincide with those of the electric field free scenario, as shown in Fig. 6(a) (iii). It is noteworthy that the cancellation of the \mathbf{E} terms in Eq. (27) is solely effective for $\varepsilon = \sum_{i=1}^N \varepsilon_i c_i$. In addition, its validity remains assured for low temperatures and weak electric fields, where c_d and c_m undergo tiny changes, and ε can still be approximated with a linear function of c .

where θ is defined by $\cos \theta = \mathbf{E} \cdot \mathbf{n} / (|\mathbf{E}| |\mathbf{n}|)$. It highlights that the equilibrium composition is also correlated with the interface orientation inside the electric field. To put it more succinctly, the system shows the anisotropic behavior within the electric field, with the equilibrium composition influenced by the orientation of the interface. This interface orientation-related anisotropic behavior will be further explored in Sec. IV E 1.

5. Interface position

Following Eq. (16), the electric field strength $\mathbf{E}(c)$ also relies on the interface position L_0 . By varying L_0 with the serial setup shown in Fig. 7(a), the magnitudes of both \mathbf{E}_d and \mathbf{E}_m soar with the increase in L_0 , as shown by the slopes of the Ψ curves in Fig. 7(b). As a result of this, the droplet equilibrium composition c_d decreases, while the matrix binodal composition c_m increases. This observed tendency aligns well with the theoretical predictions via Eq. (15). It also suggests that the equilibrium state is significantly impacted by the thickness of the phases and adds complexities to the thermodynamics of the dielectric fluids.

B. Validation of spinodal composition

In the second part, we validate our theory on the spinodal composition, which is crucial to understand the electric field-induced phase separation. Here, the droplet–matrix binary system is selected with the permittivity ratio $\nu = 40 : 1$ and conductivity ratio $s = 5 : 1$. The initial configuration is shown in Fig. 8(a) (i), where a homogeneous mixture is confined inside the 10×200 slab domain. The slab setup ensures that the spinodal decomposition produces an interface

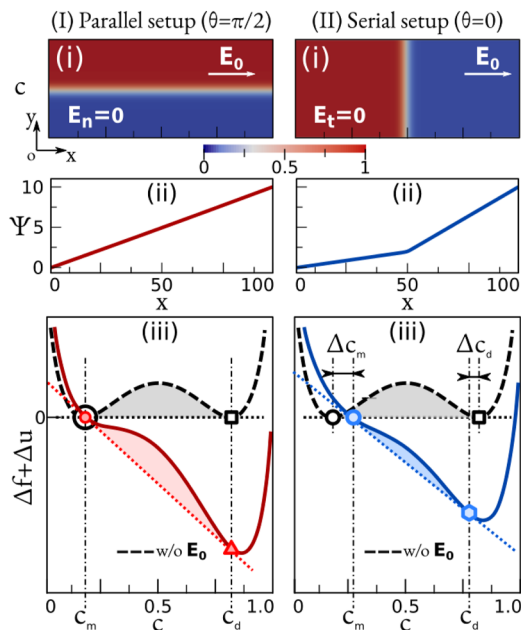


FIG. 6. Anisotropic thermodynamic equilibrium of the droplet–matrix system with (a) parallel setup: interface parallel to the external electric field strength \mathbf{E}_0 and (b) serial setup: interface perpendicular to \mathbf{E}_0 . (i) Equilibrium composition field scaled by the color bar in the following. (ii) Equilibrium electric potential in x direction at $y = 25$. (iii) Equilibrium condition with Eq. (15). Colored lines: excess total energy density $\Delta f + \Delta u$; color dots: binodal compositions inside the electric field. Black dashed lines and dots denote the excessive energy density Δf and binodal compositions with $\mathbf{E}_0 = 0$, respectively.

constrained in the serial setup, perpendicularly oriented to the electric field strength, as shown in Fig. 6(b). Consequently, the potential impact of interface orientation on thermodynamics, as discussed in Sec. IV A 4, can be mitigated.

Triggered by the thermal composition noise, the composition fluctuations are observed at time $t = 10^3$ shown in Fig. 8(a) (i) and (ii). However, by $t = 10^4$, only the initial composition $c_0 = 0.40$ entering the spinodal region results in the clearly visible phase separation, as shown in Fig. 8(a) (ii). Furthermore, by rotating the electric field by $\pi/2$, as shown in Fig. 8(a) (iii) (the parallel configuration), and applying the same parameters as Fig. 8(a) (i), the spinodal decomposition occurs at the lower initial composition $c_0 = 0.28$. Because the parallel configuration produces the composition-independent $\mathbf{E} = \mathbf{E}_0$, the spinodal region is not modified by the electric-field, which is in consistency with our theory in Eq. (20).

Moreover, at various temperatures ranging from 1.0 to 1.8, the spinodal compositions c_s are testified in simulations with the bisection method. The simulated values of c_s , marked by the colored dots, exhibit good agreement with the theoretical values calculated by Eq. (21). In addition, the spinodal compositions (black dots) for the parallel configuration revert to the electric field-free spinodal compositions; see the black dashed line. This observation again not only emphasizes the significance of the interface orientation effect but

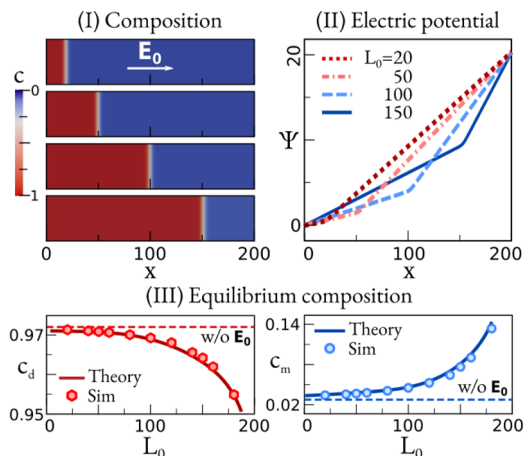


FIG. 7. Droplet–matrix interface position L_0 modifies thermodynamic equilibrium. (a) Equilibrium composition. (b) Equilibrium electric potential. (c) Binodal compositions as a function of L_0 ; left panel: equilibrium droplet composition; right panel: equilibrium matrix composition. Color dots: simulation; color lines: theory Eq. (15); dashed lines: equilibrium compositions without electric fields.

also highlights the good consistency with the theoretical calculation according to Eq. (20).

C. Phase diagram

In this section, we summarize the phase diagram of the binary leaky dielectric system, which helps determine the criterion of electric-induced phase separation affected by different conditions, including changing the dielectric materials, the mixture composition, temperature, and electric field strength. Utilizing Eqs. (15)–(18), we determine the equilibrium binodal compositions for the droplet and matrix phases at different temperatures T within various local electric field strength $|\mathbf{E}|$. As stated in the previous part, the permittivity ratio, conductivity ratio, and interface geometry of the dielectric materials can magnificently impact the thermodynamics under the invariant external electric field strength \mathbf{E}_0 ; we stress that the local electric field strength $|\mathbf{E}|$, instead of \mathbf{E}_0 , should be the appropriate freedom for the multicomponent dielectric system. Employing Eqs. (21) and (22), we also solve the spinodal composition and critical point. This yields the $T - c - |\mathbf{E}|$ phase diagram for the droplet–matrix system, which can be categorized into three distinct scenarios, as shown in Fig. 9. Notably, two critical factors contribute significantly to the construction of the phase diagram: the permittivity ratio ν and conductivity ratio s .

- (I) For $(\nu - 1)(s - 1) > 0$, with an increase in the electric field, the droplet equilibrium composition c_d decreases, while that of matrix c_m increases. It suggests that the mixing of the droplet and matrix is induced by the electric field, leading to shrinkage of the immiscible region enclosed by the blue-shaded plane shown in Fig. 9(a) (i). In addition, the spinodal composition shows a similar tendency, mirroring the changing behavior of binodal compositions. Moreover, the critical temperature, marked by the orange line, decreases

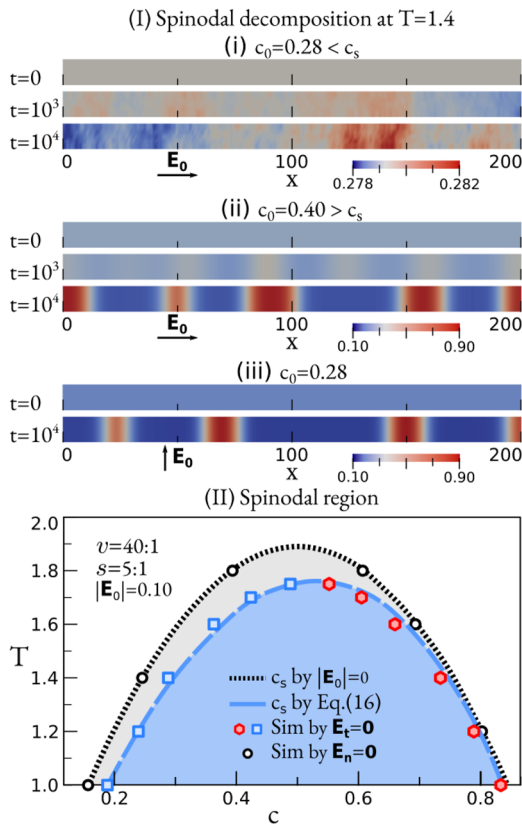


FIG. 8. Spinodal composition c_s influenced by the electric field. The parameters are given in Sec. IV B. (a) Spinodal decomposition with time t at temperature $T = 1.4$. (i) Initial composition $c_0 < c_s$ outside the spinodal region; no phase separation happens. (ii) $c_0 > c_s$ entering the spinodal region promotes the phase separation. (iii) Rotating the electric field strength direction by $\pi/2$; phase separation appears in the setup (i). The color bars scale the corresponding composition. (b) Blue-colored spinodal region modified by the external electric field. Color dots: simulated c_s ; blue dashed line: c_s with Eq. (21). Black dashed lines: c_s without the electric field. Black dots mark the simulated c_s with the parallel setup as Fig. 6(a) (i).

with $|\mathbf{E}|$, also indicating enhanced mixing of the droplet and matrix.

In Fig. 9(a) (ii), a representative phase diagram is shown for the system with $\nu = 40 : 1$ and $s = 5 : 1$ at the external electric field strength $|\mathbf{E}_0| = 0.10$. It is evident that the blue solid binodal and dashed spinodal lines deviate from the black lines representing the phase diagram without the electric field. Importantly, the deviation for the matrix phase is more pronounced than for the droplet phase. This discrepancy is attributed to the fact that the equilibrium electric field strength \mathbf{E}_m inside the matrix is stronger than \mathbf{E}_d inside the droplet. This emphasizes a crucial aspect of this work—the local electric field strength is composition-dependent, derived from Ohm's law and expressed by Eq. (14). Consequently, at the critical temperature marked by the orange dot, the critical composition c^* also increases with $|\mathbf{E}|$, equaling the equilibrium compositions and the spinodal composition, i.e., $c_d = c_m = c_s$.

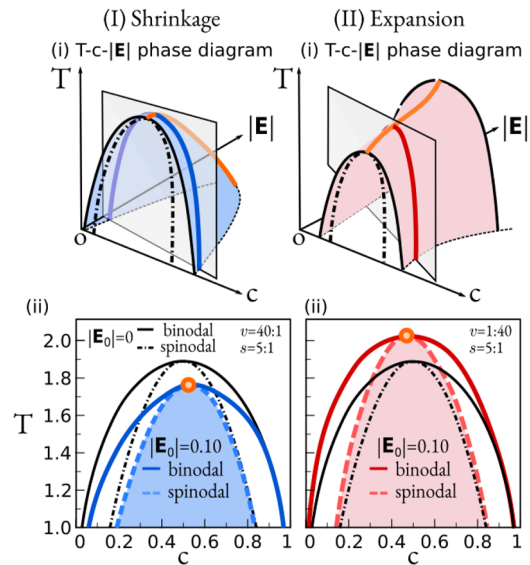


FIG. 9. Phase diagram of the binary dielectric system. (a) Immiscible region shrinks with the increase in electric field strength \mathbf{E} . (i) Illustration of the T - c - $|\mathbf{E}|$ phase diagram. Blue line: binodal position at $|\mathbf{E}| > 0$; orange line: critical points; black dashed line: binodal at $|\mathbf{E}| = 0$ black dotted-dashed curve: spinodal at $|\mathbf{E}| = 0$. (ii) Phase diagram with the permittivity ratio $\nu = 40 : 1$. Blue lines: theory with Eq. (15) at the external electric field strength $|\mathbf{E}_0| = 0.1$. Black dashed line: phase diagram at $|\mathbf{E}_0| = 0$. Orange dot: critical point. (b) Immiscible region expands with the increase in \mathbf{E} . (i) Illustration of the T - c - $|\mathbf{E}|$ phase diagram. Red line: binodal position at $|\mathbf{E}| > 0$. (ii) Phase diagram with the permittivity ratio $\nu = 1 : 40$. In all setups, the conductivity ratio is fixed as $s = 5 : 1$.

- (II) For $(\nu - 1)(s - 1) < 0$, with larger $|\mathbf{E}|$, c_d increases, and c_m decreases, showing reverse behavior compared to the previous case. In other words, demixing of the droplet and matrix is favored within the electric field. Consequently, the immiscible region expands, as depicted by the red-shaded plane shown in Fig. 9(b) (i). This expansion of the immiscible region is verified by a real binary system with $\nu = 1 : 40$, $s = 5 : 1$ and $|\mathbf{E}_0| = 0.10$ shown in Fig. 9(b) (ii). The deviation of the red solid binodal and dashed spinodal lines from the phase diagram with $|\mathbf{E}| = 0$ (see the black lines) is noticeable. Moreover, the critical point exhibits an opposite tendency from the previous case, marked by the orange dots. Here, the critical temperature increases and the critical composition decreases with $|\mathbf{E}|$, aligning with the demixing induced by the electric field.
- (III) For $(\nu - 1)(s - 1) = 0$, or when the intersection angle between the interface normal direction and \mathbf{E} , namely, $\theta = \pi/2$, there is a hidden scenario where the electric field has no impact on the thermodynamics. In this case, the phase diagram is identical to the black phase diagram at $|\mathbf{E}| = 0$ on the T - o - c plane. One can easily anticipate the influence of the electric field on the phase diagram by reformulating the theoretical spinodal composition in Eq. (21) as

$$\frac{\partial^2 f}{\partial c^2} + (\nu - 1)(s - 1) \frac{(\mathbf{E} \cos \theta)^2}{\sigma} = 0,$$

which inherently encapsulates the three scenarios discussed above. This is because the binodal line and critical points consistently exhibit similar behavior to the spinodal line when the electric field changes. All the three elements in the phase diagram, namely, binodal composition, spinodal composition, and critical point, reflect the miscibility of the droplet and matrix phases, leading to a comprehensive understanding of the fluid system response to the varying electric field.

D. Surface tension inside electric fields

1. Equilibrium interfacial tension

As discussed in the context of the phase diagram, the electric field can modify the immiscible region between the droplet and the matrix. It is reasonable to infer that the interfacial tension γ decreases when the immiscible region shrinks, and γ increases when the immiscible region expands. We suggest that the change in the interfacial tension by electric fields is a non-negligible mechanism for the dielectric breakdown. To explore this inference, we categorize the problem into the following two cases.

- (I) For the following three special cases, namely, (i) the permittivity ratio $\nu = 1$, (ii) the conductivity ratio $s = 1$, and (iii) the intersection angle $\theta = \pi/2$, the excess total energy density along the interface's normal direction is simplified as

$$\Delta f + \Delta u - \mu^e \Delta c = \Delta f - f'(c_m) \Delta c.$$

Substituting it into Eq. (25), the interfacial tension γ becomes identical to the interfacial tension without the external electric field as

$$\gamma = \gamma_0 = 2 \int_0^\infty [\Delta f - f'(c_m) \Delta c] dx. \quad (29)$$

Just as observed in the phase diagram, it is apparent that the interfacial tension remains unaffected by the presence of an electric field.

- (II) Now, we consider the more general case with $\nu \neq 1, s \neq 1$ and the interface perpendicular to the electric field. In this scenario, the interfacial tension γ is given by

$$\gamma = \gamma_0 + \gamma_e.$$

Substituting Eq. (18) into Eq. (25) the electric field contribution γ_e yields

$$\begin{aligned} \gamma_e &= 2 \int_0^\infty [\Delta u - u'(c_m) \Delta c] dx \\ &= - \int_0^L \left[\left(\frac{\partial \varepsilon}{\partial c} / \frac{\partial \sigma}{\partial c} \right) \left(\frac{\mathbf{J}^2}{\sigma} - \frac{\mathbf{J}^2}{\sigma_m} \right) + \frac{\partial \varepsilon}{\partial c} \frac{\Delta c}{\sigma_m^2} \mathbf{J}^2 \right] dx \\ &= - \int_0^L \frac{\partial \varepsilon}{\partial c} \frac{\partial \sigma}{\partial c} \frac{\Delta c^2}{\sigma(c) \sigma_m^2} \mathbf{J}^2 dx \\ &= - \frac{\partial \varepsilon}{\partial c} \frac{\partial \sigma}{\partial c} \mathbf{I} \mathbf{E}_0^2, \end{aligned} \quad (30)$$

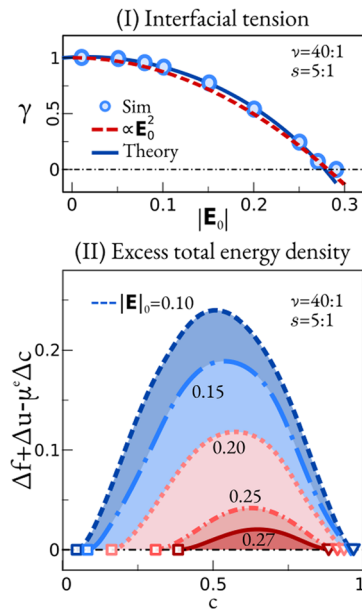


FIG. 10. (a) Interfacial tension with the external electric field strength \mathbf{E}_0 . Dots: simulation; red dashed line: parabolic fitting; blue solid line: theory with Eq. (32). (b) Excess total energy density $\Delta f + \Delta u - \mu^e \Delta c$ with \mathbf{E}_0 . Colored squares: equilibrium matrix composition; colored triangles: equilibrium droplet composition.

in which \mathbf{I} is a positive integral as

$$\mathbf{I} = 4 \left(\frac{\sigma_d}{\sigma_m + \sigma_d} \right)^2 \int_0^L \frac{(\Delta c)^2}{\sigma(c)} dx.$$

Therefore, the interfacial tension decreases in a parabolic relation with the increasing external field strength,

$$\gamma = \gamma_0 - \frac{\partial \varepsilon}{\partial c} \frac{\partial \sigma}{\partial c} \mathbf{I} \mathbf{E}_0^2 = \gamma_0 - (\nu - 1)(s - 1) \mathbf{I} \mathbf{E}_0^2. \quad (31)$$

It needs to be addressed that Eq. (31) can only qualitatively express the influence of the electric field on the interfacial tension.

As shown in Fig. 10(a), the simulated interfacial tension γ as a function of \mathbf{E}_0 matches the parabolic relationship almost perfectly. However, the slope of $\gamma \sim \mathbf{E}_0^2$ is a magnitude smaller than the prefactor $(\nu - 1)(s - 1)$. The reason for this discrepancy is that γ_0 in Eq. (31) is not a constant, representing the chemical energy contribution to the interfacial tension influenced by \mathbf{E}_0 as well. Because the chemical energy and electric energy are coupled by the electrochemical potential μ , an increase in \mathbf{E}_0 leads to the equilibrium composition variance, shown by the colored dots in Fig. 10(b). Hence, the excess chemical energy density Δf should increase at the interface region to coordinate the decrease in the excess electric energy density $\Delta u \propto -\mathbf{E}_0^2$.

A more comprehensive understanding is achieved via analyzing the dependency of the interfacial tension on the excess total energy

density $\Delta f + \Delta u - \mu^e \Delta c$. Based on Eq. (25), the interfacial tension can also be expressed as (deduction in A)

$$\gamma = \int_{c_m}^{c_d} \sqrt{2\kappa(\Delta f + \Delta u - \mu^e \Delta c)} dc. \quad (32)$$

As clearly shown in Fig. 10(b), by varying $|\mathbf{E}_0|$ from 0.10 to 0.27, the excess total energy $\Delta f + \Delta u - \mu^e \Delta c$ decreases with the electric field, resulting in the interfacial tension γ decreasing with $|\mathbf{E}_0|$. To verify our theory, Eq. (32) is numerically calculated and plotted in Fig. 10(a) with the blue solid line, and good agreement with simulated γ (dots) is observed.

2. Surface tension thinning/thickening effect

Based on the parabolic relation in Eq. (31), both the permittivity ratio and the conductivity ratio play crucial roles in the interfacial tension changing with the electric field. There is no wonder that the prefactor $(\nu - 1)(s - 1)$ shows again, identical to the prefactor in Eqs. (21) and (22) to determine the spinodal composition and critical point. Because the interfacial tension and phase separation are all intrinsically connected to the excess total free-energy $\Delta f + \Delta u - \mu^e \Delta c$.

In this way, we can qualitatively consider the interfacial tension changed by the electric field into three categories. (I) For $(\nu - 1)(s - 1) > 0$, the interfacial tension decreases with the enhancing electric field. This usually happens in numerous binary systems, such as water–air and mercury–air, where the conductivity ratio $s \gg 1$ and the permittivity ratio $\nu > 1$. Therefore, with an increased electric field, the interfacial tension experiences a thinning effect. (II) Conversely, for $(\nu - 1)(s - 1) < 0$, the interfacial tension increases with the electric field. Especially, for certain polymer–air systems, the conductivity ratio $s \ll 1$ and the permittivity ratio $\nu > 1$, the interfacial tension thickening effect takes place. (III) For $(\nu - 1)(s - 1) = 0$, it is a rare case that two pure materials possess identical permittivity or conductivity.

E. Dynamics

In this section, we briefly talk about the dynamics of the dielectric fluids inside the electric field from the thermodynamic perspective. Here, two special scenarios are considered, namely, the electrostriction and the dielectric breakdown.

1. Electrostriction

The first classical study case is the electrostriction of the droplet, which has been intensively investigated.¹⁸ Once placed into an electric field, the droplet molecules get polarized and stretched/suppressed, leading to a deformed shape deviating from a perfect sphere. To elucidate the droplet deformation, we may first look at the droplet–matrix interfacial tension inside the electric field. In our previous discussion in Sec. IV A 4, we suggest that the interface orientation changes the equilibrium composition for each phase. Therefore, the droplet–matrix interfacial tension also exhibits anisotropic behaviors as

$$\gamma = \gamma_0 - \alpha(\mathbf{E} \cos \theta)^2. \quad (33)$$

Here, the parameter α can be determined by fitting Eq. (32) with the parabolic fitting. Notably, the factor α depends on the permittivity

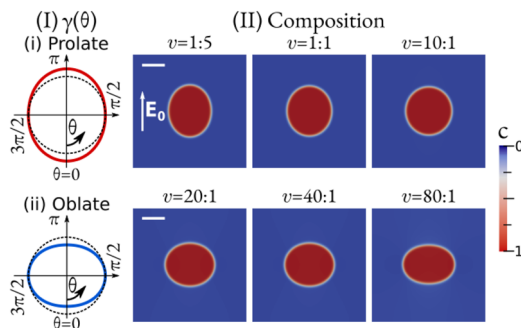


FIG. 11. (a) Two stable droplet shapes inside the electric field depending on orientation-related interfacial tension γ as a function of θ , which is the intersection angle between external electric field strength \mathbf{E}_0 and the interface normal direction \mathbf{n} . (i) Prolate; (ii) oblate. (b) Simulated droplet morphologies with increasing permittivity ratio ν . The color bar measures the droplet composition, and the white scale bar denotes 40.

ratio ν and conductivity ratio s , which results in two different equilibrium droplet shapes, namely, the prolate and the oblate, as shown in Fig. 11(a).

For the prolate drops, the interfacial tension maximum exists at $\theta = 0$ or π , where the interface is perpendicular to the electric field. As θ approaches $\pi/2$ or $3\pi/2$, γ reaches its minima. For the oblate drops, the interfacial tension has minima at $\theta = 0$ or π and reaches its maxima at $\pi/2$ or $3\pi/2$. In this way, according to the constant Young–Laplace pressure at equilibrium in 2 dimensions, $\Delta p = \gamma/r$, the interface radius r becomes also orientation-related as

$$r = \frac{\gamma_0 - \alpha(\mathbf{E} \cos \theta)^2}{\Delta p}.$$

This relation serves only as a phenomenological description of the electrostriction behaviors, since the parabolic $\gamma \propto (\mathbf{E} \cos \theta)^2$ is derived for the flat interface.

By a curved droplet interface, the surrounding electric field becomes more complicated, and Eq. (33) is not capable of measuring the interface tension precisely. An improved analytical model to calculate the equilibrium droplet shape has been already established by Taylor and Feng.^{19,49} Their theories point out the critical transition from prolate to oblate shapes appears at $\nu = 10.3$ for $s = 5$. As shown in Fig. 11(b), the simulated critical transition occurs around $\nu = 10$, which is in accordance with the theories of Taylor and Feng. The critical transition at $\nu = 10.3$ also indicates that the prefactor α is not proportional to $(\nu - 1)$, but should take a more complex formulation.

2. Dielectric breakdown

Now, we arrive at the dielectric breakdown of the droplet–matrix system. In this scenario, increasing the electric field deforms the droplet phases, so that the left and right electrodes are connected by the deformed fluids. This unfavored phenomenon destroys the proper functions of dielectric devices and has a magnificent meaning for the performance of electronic equipment.

First, to simulate the dielectric breakdown, we placed the equilibrium droplet–matrix bi-layers with the serial configuration into

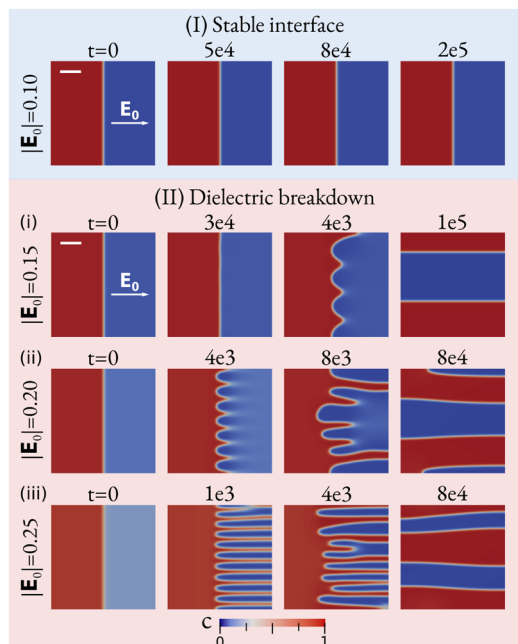


FIG. 12. Dielectric breakdown with increasing external electric field strength $|E_0|$. (a) Stable droplet–matrix interface inside the weak electric field. (b) The evolution of fingering morphologies ends with the dielectric breakdown. The color bar measures the droplet composition, and the white scale bar denotes 40.

the electric field, as shown in Fig. 7(a). With the increase in electric field strength $|E_0|$ above 0.15, the interface becomes unstable. We suggest that this instability emanates from the interfacial tension reduction with increasing the electric field strength. At large $|E_0|$, the electric energy reduces the interfacial tension, forming the wide interface, which is due to the balance between the decreasing interfacial tension and the increasing dielectric forces. Notably, when the thermal noises exist, the composition fluctuation results in the interface perturbation, which obeys the capillary wave theory.⁵⁰ The amplitude of the capillary wave ($\Delta^2 h$) is inversely proportional to the interfacial tension as

$$\langle \Delta^2 h \rangle \propto \frac{R_g T}{\gamma}.$$

Due to the reduction in γ with $|E_0|$, thermal noises trigger the interface instability, giving rise to the red droplet phase forming fingering morphologies shown in Fig. 12(b).

Furthermore, as analyzed in Sec. IV A 5, when the fingertip is approaching the right boundary, the interface position L_0 increases, so that the electric field has more impact on the tip area, promoting the mixing of the droplet with the matrix; as shown in Fig. 7(c). Hence, the interfacial tension continuously decreases, which further intensifies the instability. Finally, the red droplet fingers connect the left and right boundaries and the dielectric layer breaks down.

By comparing the fingering to the classical Rayleigh–Taylor instability and Saffmann–Taylor instability, we suggest that the

dielectric breakdown is highly associated with the interface instability, which is associated with the permittivity difference between droplet and matrix, as expressed in Eq. (31). As shown in Fig. 12(b), more fingertips emerge with increasing $|E_0|$. It indicates that a critical wavelength decides the dynamics of the dielectric breakdown, which needs to be studied in future studies.

In addition, the fingering morphologies shown in Fig. 12(b) also resemble the shape of the Taylor cone,⁵¹ which forms during the electrospinning process and has been widely studied in experiments. As our electrohydrodynamic CHNSG model is capable of coupling the hydrodynamics with electrostatics, we hope to elucidate the more complex mechanisms of the Taylor cone formation in a forthcoming work.

Second, from the perspective of energy minimization, we may elucidate the dielectric breakdown as follows. The dielectric breakdown is equivalent to the morphological transition from the serial configuration to the parallel configuration, as shown in Figs. 13(a) and 13(b). Therefore, we rewrite the total energy of the dielectric fluids at the initial state, as shown in Figs. 13(a) (i) and (b) (ii), expressing it into a sum of the bulk and interface energy terms as

$$G = (f_b + u_b) V + \gamma S,$$

where V stands for the fluid volume and S denotes the initial droplet–matrix interface area. Especially as the setups shown in Figs. 13(a) (i) and (b) (ii), we have $V = L \times W$ (length by width), and $S = W$. After the dielectric breakdown, the total energy can be written as

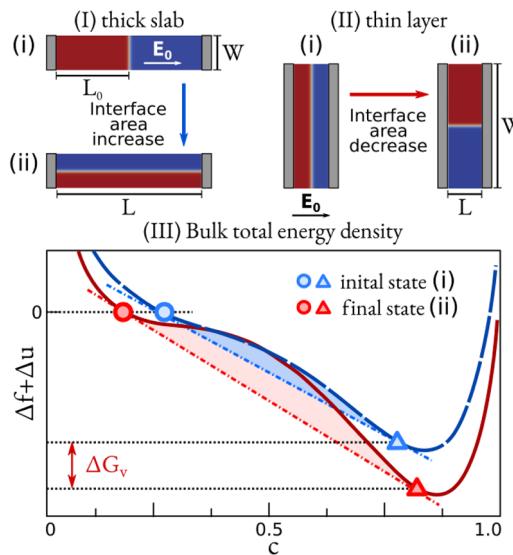


FIG. 13. Illustration of dielectric breakdown with two types of configuration. (a) The thick slab has interface area increase after the dielectric breakdown. (i) Initial state; (ii) final state. (b) The thin layer has interface area reduction after the dielectric breakdown. (c) Bulk total energy density $\Delta f + \Delta u$ (colored lines) changes after the dielectric breakdown. The colored dots mark the equilibrium compositions, which are determined by the dotted–dashed common tangent lines. Blue: the initial state; red: the final state.

$$G' = (f'_b + u'_b) V + \gamma' S'$$

It should be noted that at the final state, the interfacial tension is identical to $\gamma' = \gamma_0$ in Eq. (29), and the interface area S' equates to the electrode distance L . Hence, the occurrence of the dielectric breakdown demands the energy decrease as

$$\begin{aligned} G' - G &= [(f'_b + u'_b) - (f_b + u_b)] V + \gamma' S' - \gamma S \\ &= -(\Delta f + \Delta u) V + \gamma' S' - \gamma S \\ &= -\Delta G_v L_0 W + \gamma_0 L - \gamma W \leq 0. \end{aligned}$$

Taking the matrix phase as zero energy reference, the bulk total energy density difference ΔG_v is shown in Fig. 13(c), and the minus sign indicates that the dielectric breakdown can minimize the bulk total energy. After simplification, we derive the critical aspect ratio, which spontaneously initiates the dielectric breakdown, if

$$\frac{W}{L} \geq \frac{\gamma_0}{\Delta G_v L_0 + \gamma}.$$

Here, we suggest that the device aspect ratio W/L is a key factor that influences the dielectric breakdown. As shown in Fig. 13(c), the total bulk energy always decreases, for its energy density variance $-\Delta G_v < 0$ is not changeable with W/L . However, the interfacial energy changes depend on the aspect ratio. For the initial thick slab shown in Fig. 13(a), where the distance between the electrodes L is much larger than the electrode width W , the interfacial area increases drastically from W to L . Meanwhile, the interfacial tension also increases, which is positively correlated with the color-shaded area shown in Fig. 13(c); see Eq. (32). With the principle of energy minimization, the dielectric breakdown can only be achieved when the bulk total energy decrease overwhelms the interfacial energy increase. Otherwise, the dielectric breakdown will be suppressed. On the contrary, for the thin layer setup shown in Fig. 13(b), where W direction is larger than L , the dielectric breakdown always tends to reduce the interface area from W to L . Even though the interfacial tension increases during the transition, dielectric breakdown is more prone to occur than the thick slab configuration shown in Fig. 13(a).

The preceding analysis, grounded in the energy minimization principle, explains our simulation results shown in Fig. 12(b). At $|\epsilon_0| = 0.15$, dielectric breakdown occurs, and the interface becomes unstable, even though the interfacial tension remains nonzero; see Fig. 10(a). Consequently, the dielectric breakdown is determined by the interface instability, which is influenced by the cooperative interplay of chemical free energy, electric field, and device geometry.

V. CONCLUSION

In conclusion, we have systematically investigated the thermodynamic equilibrium of the multicomponent *leaky* dielectric materials. Starting from the total energy functional, we present the methodology to deduce the theoretical expressions for the equilibrium composition, spinodal composition, critical

points, and critical electric field strength. Our methodology can also be applied for multicomponent systems, such as intercalation materials in Li-ion batteries. The comprehensive analysis enables us to study the electric field-induced phase separation by constructing the theoretical phase diagrams, where three crucial state parameters, the composition c , the temperature T , and the electric field strength E , play pivotal roles. The accuracy of the theoretical phase diagram has been validated through phase-field simulations. Notably, our study involved revisiting the expressions for several key thermodynamic quantities, resulting in rigorous formulations for the excess electric energy density and spinodal composition. Moreover, we analyzed the equilibrium conditions for the dielectric materials, shedding light on previously overlooked geometry factors, including interface orientation and position. Furthermore, we extended our investigation to dynamic aspects of dielectric behavior, discussing two interesting phenomena: (I) the electrostriction of droplets and (II) dielectric breakdown. Our analysis implies that both phenomena are highly correlated with the interfacial tension, which is altered not only by the electric field but also by the material properties, such as permittivity and conductivity. We anticipate this fundamental study to serve as a benchmark for future research on multicomponent dielectric materials, providing valuable insights into the thermodynamic and kinetic behaviors.

ACKNOWLEDGMENTS

H. Zhang thanks the Gottfried-Wilhelm Leibniz prize NE 822/31-1 of the German Research Foundation (DFG) for funding this research. F. Wang acknowledges the VirtMat project P09 of the Helmholtz Association (MSE-programme No. 43.31.01). The authors acknowledge support from the state of Baden-Wuerttemberg through bwHPC.

AUTHOR DECLARATIONS

Conflict of Interest

The authors have no conflicts to disclose.

Author Contributions

Haodong Zhang: Conceptualization (equal); Formal analysis (equal); Funding acquisition (equal); Investigation (equal); Validation (equal); Visualization (equal); Writing – original draft (equal). **Fei Wang:** Formal analysis (equal); Investigation (equal); Methodology (equal); Supervision (equal); Writing – original draft (equal); Writing – review & editing (equal). **Britta Nestler:** Funding acquisition (lead); Project administration (lead); Resources (lead); Software (lead); Supervision (equal); Writing – review & editing (supporting).

DATA AVAILABILITY

The data that support the findings of this study are available from the corresponding author upon reasonable request.

NOMENCLATURE

List of symbols: Notation description

$\langle \Delta h^2 \rangle$	Capillary wave amplitude
\mathcal{F}	Chemical free energy functional
\mathcal{K}	Kinetic energy
\mathcal{L}	Total energy functional
\mathcal{U}	Electric potential energy
\mathbf{c}	Composition vector
c^*	Concentration of critical point
c_d	Equilibrium droplet concentration
c_i	Concentration of composition i
c_m	Equilibrium matrix concentration
c_s	Spinodal concentration
D	Diffusivity
\mathbf{E}	Local electric field strength
\mathbf{E}_0	External electric field strength
ε	Permittivity
f	Bulk chemical free energy density
g	Chemical free energy density functional
\mathbf{J}	Current density
\mathbf{M}	Mobility
\mathbf{n}	Normal vector of the droplet-matrix interface
N	Number of components
p	Pressure
R_g	Gas constant
s	Conductivity ratio between droplet and matrix
T	Temperature
t	Time
T^*	Temperature of critical point
T_r	Reference temperature
u	Electrical energy density
\mathbf{u}	Macroscopic fluid velocity
v_m	Molar volume
\mathbf{x}	Position vector
γ	Interfacial tension
δ_{ij}	Kronecker's delta
Δt	Simulation time step
Δx	Mesh resolution
η	Dynamic viscosity
θ	Intersection angle of \mathbf{E}_0 with \mathbf{n}
κ	Interfacial tension parameter
μ^e	Equilibrium electrochemical
μ_i	Electrochemical potential of composition i
ν	Permittivity ratio between droplet and matrix
ξ_i	Thermal composition noise amplitude
ρ	Density
ρ_e	Charge density
σ	Conductivity
χ	Flory interaction parameter
Ψ	Electric potential

APPENDIX: INTERFACIAL TENSION

Here, we deduce the formulation of the interfacial tension in Eq. (32). For a one dimensional case, the equilibrium condition fulfills Eq. (24) as

$$\frac{\partial f}{\partial c} + \frac{\partial u}{\partial c} - \kappa \frac{\partial^2 c}{\partial x^2} = \mu^e. \quad (\text{A1})$$

Multiplying $\partial c/\partial x$ on each side of Eq. (A1), we have

$$\frac{\partial f}{\partial x} + \frac{\partial u}{\partial c} \frac{\partial c}{\partial x} - \frac{\partial^2 c}{\partial x^2} \frac{\partial c}{\partial x} = \mu^e \frac{\partial c}{\partial x}. \quad (\text{A2})$$

Integrating Eq. (A2) from 0 to x , we obtain

$$\int_0^x \left(\frac{\partial f}{\partial x} - \mu^e \frac{\partial c}{\partial x} \right) dx + \int_{c_m}^c \frac{\partial u}{\partial c} dc = \int_0^x \kappa \frac{\partial^2 c}{\partial x^2} \frac{\partial c}{\partial x} dx,$$

resulting in the following relation:

$$f|_0^x + \Delta u|_0^x - \mu^e c|_0^x = \frac{\kappa}{2} \left(\frac{\partial c}{\partial x} \right)^2 \Big|_0^x.$$

The position $x = 0$ denotes the bulk matrix region where we have the chemical free-energy $f = f(c_m)$ and the composition reaches the equilibrium matrix composition $c = c_m$. Especially, the term $\Delta u = 0$ at $x = 0$ because $x = 0$ is defined as the zero potential position; see Eq. (18). Moreover, inside the bulk matrix region, there is no composition gradient so that $\partial c/\partial x = 0$.

Hence, we obtain the following expression for the excess total energy density equal to the interfacial energy term as

$$\Delta f + \Delta u - \mu^e \Delta c = \frac{\kappa}{2} \left(\frac{\partial c}{\partial x} \right)^2.$$

The equilibrium composition gradient at the position x reads

$$\frac{\partial c}{\partial x} = \sqrt{\frac{2(\Delta f + \Delta u - \mu^e \Delta c)}{\kappa}}. \quad (\text{A3})$$

Here, the positive root is taken because the droplet composition c rises from c_m to c_d along the x axis. Substituting Eq. (A3) into Eq. (25), we recover the theoretical interfacial tension Eq. (32) as

$$\begin{aligned} \gamma &= 2 \int_0^L [\Delta f + \Delta u - \mu^e \Delta c] dx \\ &= 2 \int_{c_m}^{c_d} \frac{\Delta f + \Delta u - \mu^e \Delta c}{\partial c/\partial x} dc \\ &= \int_{c_m}^{c_d} \sqrt{2\kappa (\Delta f + \Delta u - \mu^e \Delta c)} dc. \end{aligned}$$

REFERENCES

- M. S. Patil, J.-H. Seo, and M.-Y. Lee, "A novel dielectric fluid immersion cooling technology for Li-ion battery thermal management," *Energy Convers. Manage.* **229**, 113715 (2021).
- P. Shi, J. Ma, M. Liu, S. Guo, Y. Huang, S. Wang, L. Zhang, L. Chen, K. Yang, X. Liu *et al.*, "A dielectric electrolyte composite with high lithium-ion conductivity for high-voltage solid-state lithium metal batteries," *Nat. Nanotechnol.* **18**, 602–610 (2023).
- S. J. Fiedziuszko, I. C. Hunter, T. Itoh, Y. Kobayashi, T. Nishikawa, S. N. Stitzer, and K. Wakino, "Dielectric materials, devices, and circuits," *IEEE Trans. Microwave Theory Tech.* **50**, 706–720 (2002).
- W. Lou, M. Mao, K. Song, K. Xu, B. Liu, W. Li, B. Yang, Z. Qi, J. Zhao, S. Sun *et al.*, "Low permittivity cordierite-based microwave dielectric ceramics for 5G/6G telecommunications," *J. Eur. Ceram. Soc.* **42**, 2820–2826 (2022).
- M. Visokay, J. Chambers, A. Rotondaro, A. Shanware, and L. Colombo, "Application of HfSiON as a gate dielectric material," *Appl. Phys. Lett.* **80**, 3183–3185 (2002).

- ⁶D. Ji, T. Li, W. Hu, and H. Fuchs, "Recent progress in aromatic polyimide dielectrics for organic electronic devices and circuits," *Adv. Mater.* **31**, 1806070 (2019).
- ⁷K. Zou, Y. Dan, H. Xu, Q. Zhang, Y. Lu, H. Huang, and Y. He, "Recent advances in lead-free dielectric materials for energy storage," *Mater. Res. Bull.* **113**, 190–201 (2019).
- ⁸X.-J. Liu, M.-S. Zheng, G. Chen, Z.-M. Dang, and J.-W. Zha, "High-temperature polyimide dielectric materials for energy storage: Theory, design, preparation and properties," *Energy Environ. Sci.* **15**, 56–81 (2022).
- ⁹N. Baskaran, A. Ghule, C. Bhongale, R. Murugan, and H. Chang, "Phase transformation studies of ceramic BaTiO₃ using thermo-Raman and dielectric constant measurements," *J. Appl. Phys.* **91**, 10038–10043 (2002).
- ¹⁰Y.-Z. Tang, Z.-F. Gu, J.-B. Xiong, J.-X. Gao, Y. Liu, B. Wang, Y.-H. Tan, and Q. Xu, "Unusual sequential reversible phase transitions containing switchable dielectric behaviors in cyclopentyl ammonium 18-crown-6 perchlorate," *Chem. Mater.* **28**, 4476–4482 (2016).
- ¹¹Y. Jin, N. Xia, and R. A. Gerhardt, "Enhanced dielectric properties of polymer matrix composites with BaTiO₃ and mwcnt hybrid fillers using simple phase separation," *Nano Energy* **30**, 407–416 (2016).
- ¹²X. Liu, B. Xie, C. Duan, Z. Wang, B. Fan, K. Zhang, B. Lin, F. J. Colberts, W. Ma, R. A. Janssen *et al.*, "A high dielectric constant non-fullerene acceptor for efficient bulk-heterojunction organic solar cells," *J. Mater. Chem. A* **6**, 395–403 (2018).
- ¹³Y. Ji, C. Pan, M. Zhang, S. Long, X. Lian, F. Miao, F. Hui, Y. Shi, L. Larcher, E. Wu, and M. Lanza, "Boron nitride as two dimensional dielectric: Reliability and dielectric breakdown," *Appl. Phys. Lett.* **108**, 012905 (2016).
- ¹⁴F. Palumbo, C. Wen, S. Lombardo, S. Pazos, F. Aguirre, M. Eizenberg, F. Hui, and M. Lanza, "A review on dielectric breakdown in thin dielectrics: Silicon dioxide, high-k, and layered dielectrics," *Adv. Funct. Mater.* **30**, 1900657 (2020).
- ¹⁵K. Bertoldi and M. Gei, "Instabilities in multilayered soft dielectrics," *J. Mech. Phys. Solids* **59**, 18–42 (2011).
- ¹⁶H. S. Park, Q. Wang, X. Zhao, and P. A. Klein, "Electromechanical instability on dielectric polymer surface: Modeling and experiment," *Comput. Methods Appl. Mech. Eng.* **260**, 40–49 (2013).
- ¹⁷L. Dorfmann and R. W. Ogden, "Instabilities of soft dielectrics," *Philos. Trans. R. Soc., A* **377**, 20180077 (2019).
- ¹⁸G. I. Taylor, "Electrically driven jets," *Proc. R. Soc. London, Ser. A* **313**, 453–475 (1969).
- ¹⁹J. Melcher and G. Taylor, "Electrohydrodynamics: A review of the role of interfacial shear stresses," *Annu. Rev. Fluid Mech.* **1**, 111–146 (1969).
- ²⁰R. J. Turnbull and J. R. Melcher, "Electrohydrodynamic Rayleigh-Taylor bulk instability," *Phys. Fluids* **12**, 1160–1166 (1969).
- ²¹H. Hori, O. Urakawa, O. Yano, and Q. Tran-Cong-Miyata, "Phase separation of binary polymer mixtures under an electric field," *Macromolecules* **40**, 389–394 (2007).
- ²²G. Chen, J. Guo, J. Nie, and G. Ma, "Preparation, characterization, and application of PEO/HA core shell nanofibers based on electric field induced phase separation during electrospinning," *Polymer* **83**, 12–19 (2016).
- ²³C.-H. Wang, P. Chen, and C.-Y. D. Lu, "Phase separation of thin-film polymer mixtures under in-plane electric fields," *Phys. Rev. E* **81**, 061501 (2010).
- ²⁴C. Liedel, C. W. Pester, M. Ruppel, V. S. Urban, and A. Böker, "Beyond orientation: The impact of electric fields on block copolymers," *Macromol. Chem. Phys.* **213**, 259–269 (2012).
- ²⁵A. Roy and P.-R. Cha, "Electric field induced charge migration and formation of conducting filament during resistive switching in electrochemical metallization (ECM) memory cells," *J. Appl. Phys.* **128**, 205102 (2020).
- ²⁶G. Han and Q. Hu, "Effects of electric field on saturated vapor pressure," *J. Phys. Chem. C* **124**, 1820–1826 (2019).
- ²⁷D. Fraggedakis, M. Mirzadeh, T. Zhou, and M. Z. Bazant, "Dielectric breakdown by electric-field induced phase separation," *J. Electrochem. Soc.* **167**, 113504 (2020).
- ²⁸S. Safaripour, G. Anand, and C. Snoeyink, "Thermodynamic analysis of capillary and electric field effects on liquid-vapor equilibrium: A study on the water-ethanol mixture," *J. Phys. Chem. B* **127**, 9181–9190 (2023).
- ²⁹Q. Zhang and X. He, "Complex effects of the external electric fields on the phase separation of polymer blends," *Macromolecules* **57**, 597 (2024).
- ³⁰H. Zhang, F. Wang, and B. Nestler, "Multi-component electro-hydro-thermodynamic model with phase-field method. I. Dielectric," *J. Comput. Phys.* **505**, 112907 (2024).
- ³¹N. Nadkarni, T. Zhou, D. Fraggedakis, T. Gao, and M. Z. Bazant, "Modeling the metal-insulator phase transition in Li_xCoO₂ for energy and information storage," *Adv. Funct. Mater.* **29**, 1902821 (2019).
- ³²M. G. Verde, L. Baggetto, N. Balke, G. M. Veith, J. K. Seo, Z. Wang, and Y. S. Meng, "Elucidating the phase transformation of Li₄Ti₅O₁₂ lithiation at the nanoscale," *ACS Nano* **10**, 4312–4321 (2016).
- ³³W. Sun, B. Gao, M. Chi, Q. Xia, J. J. Yang, H. Qian, and H. Wu, "Understanding memristive switching via in situ characterization and device modeling," *Nat. Commun.* **10**, 3453 (2019).
- ³⁴H. Zhang, F. Wang, and B. Nestler, "Janus droplet formation via thermally induced phase separation: A numerical model with diffusion and convection," *Langmuir* **38**, 6882–6895 (2022).
- ³⁵F. Wang, H. Zhang, Y. Wu, and B. Nestler, "A thermodynamically consistent diffuse interface model for the wetting phenomenon of miscible and immiscible ternary fluids," *J. Fluid Mech.* **970**, A17 (2023).
- ³⁶D. Saville, "Electrohydrodynamics: The Taylor-Melcher leaky dielectric model," *Annu. Rev. Fluid Mech.* **29**, 27–64 (1997).
- ³⁷H. Zhang, Y. Wu, F. Wang, F. Guo, and B. Nestler, "Phase-field modeling of multiple emulsions via spinodal decomposition," *Langmuir* **37**, 5275–5281 (2021).
- ³⁸F. Wang, P. Altschuh, A. M. Matz, J. Heimann, B. S. Matz, B. Nestler, and N. Jost, "Phase-field study on the growth of magnesium silicide occasioned by reactive diffusion on the surface of Si-foams," *Acta Mater.* **170**, 138–154 (2019).
- ³⁹P. C. Hohenberg and B. I. Halperin, "Theory of dynamic critical phenomena," *Rev. Mod. Phys.* **49**, 435 (1977).
- ⁴⁰H. Zhang, F. Wang, L. Ratke, and B. Nestler, "Brownian motion of droplets induced by thermal noise," *Phys. Rev. E* **109**, 024208 (2024).
- ⁴¹F. Wang, B. Nestler *et al.*, "Wetting and contact-angle hysteresis: Density asymmetry and van der Waals force," *Phys. Rev. Lett.* **132**, 126202 (2024).
- ⁴²A. Milewska, K. Świerczek, J. Tobola, F. Boudoire, Y. Hu, D. Bora, B. Mun, A. Braun, and J. Molenda, "The nature of the nonmetal-metal transition in Li_xCoO₂ oxide," *Solid State Ionics* **263**, 110–118 (2014).
- ⁴³A. Vasileiadis, N. J. de Klerk, R. B. Smith, S. Ganapathy, P. P. R. Harks, M. Z. Bazant, and M. Wagemaker, "Toward optimal performance and in-depth understanding of spinel Li₄Ti₅O₁₂ electrodes through phase field modeling," *Adv. Funct. Mater.* **28**, 1705992 (2018).
- ⁴⁴J. C. Gonzalez-Rosillo, M. Balaish, Z. D. Hood, N. Nadkarni, D. Fraggedakis, K. J. Kim, K. M. Mullin, R. Pfenninger, M. Z. Bazant, and J. L. Rupp, "Lithium-battery anode gains additional functionality for neuromorphic computing through metal-insulator phase separation," *Adv. Mater.* **32**, 1907465 (2020).
- ⁴⁵W. Zhang, Y. Chen, C. Xu, C. Lin, J. Tao, Y. Lin, J. Li, O. V. Kolosov, and Z. Huang, "Tunable electrical field-induced metal-insulator phase separation in LiCoO₂ synaptic transistor operating in post-percolation region," *Nano Energy* **108**, 108199 (2023).
- ⁴⁶R. Amin and Y.-M. Chiang, "Characterization of electronic and ionic transport in Li_{1-x}Ni_{0.33}Mn_{0.33}Co_{0.33}O₂(NMC₃₃₃) and Li_{1-x}Ni_{0.50}Mn_{0.20}Co_{0.30}O₂(NMC₅₂₃) as a function of Li content," *J. Electrochem. Soc.* **163**, A1512 (2016).
- ⁴⁷D. Young, A. Ransil, R. Amin, Z. Li, and Y.-M. Chiang, "Electronic conductivity in the Li_{4/3}Ti_{5/3}O₄-Li_{7/3}Ti_{5/3}O₄ system and variation with state-of-charge as a Li battery anode," *Adv. Energy Mater.* **3**, 1125–1129 (2013).
- ⁴⁸F. Wang and B. Nestler, "Wetting transition and phase separation on flat substrates and in porous structures," *J. Chem. Phys.* **154**, 094704 (2021).
- ⁴⁹J. Q. Feng, "A 2D electrohydrodynamic model for electrorotation of fluid drops," *J. Colloid Interface Sci.* **246**, 112–121 (2002).
- ⁵⁰H. T. Davis, "Capillary waves and the mean field theory of interfaces," *J. Chem. Phys.* **67**, 3636–3641 (1977).
- ⁵¹Z. Wang, Y. Tian, C. Zhang, Y. Wang, and W. Deng, "Massively multiplexed electrohydrodynamic tip streaming from a thin disc," *Phys. Rev. Lett.* **126**, 064502 (2021).